Model Hamiltonian and time reversal breaking topological phases of antiferromagnetic half-Heusler materials

Jiabin Yu, Binghai Yan, and Chao-Xing Liu

Phys. Rev. B **95**, 235158 — Published 30 June 2017

DOI: 10.1103/PhysRevB.95.235158

Model Hamiltonian and Time Reversal Breaking Topological Phases of Anti-ferromagnetic Half-Heusler Materials

Jiabin Yu,[1] Binghai Yan,[2] and Chao-Xing Liu[1,*]

[1] *Department of Physics, the Pennsylvania State University, University Park, PA, 16802*
[2] *Department of Condensed Matter Physics, Weizmann Institute of Science, Rehovot, 7610001, Israel*

In this work, we construct a generalized Kane model with a new coupling term between itinerant electron spins and local magnetic moments of anti-ferromagnetic ordering in order to describe the low energy effective physics in a large family of anti-ferromagnetic half-Heusler materials. Topological properties of this generalized Kane model is studied and a large variety of topological phases, including Dirac semimetal phase, Weyl semimetal phase, nodal line semimetal phase, type-B triple point semimetal phase, topological mirror (or glide) insulating phase and anti-ferromagnetic topological insulating phase, are identified in different parameter regions of our effective models. In particular, we find that the system is always driven into the anti-ferromagnetic topological insulator phase once a bulk band gap is open, irrespective of the magnetic moment direction, thus providing a robust realization of anti-ferromagentic topological insulators. Furthermore, we discuss the possible realization of these topological phases in realistic anti-ferromagnetic half-Heusler materials. Our effective model provides a basis for the future study of physical phenomena in this class of materials.

I. Introduction

The discovery of time reversal invariant topological insulators (TIs)[1,2] provides us the first example of a novel topological state that is protected by certain types of symmetry (time reversal symmetry), and greatly deepens our understanding of the role of symmetry and topology in electronic band structures of solid materials. Soon after this discovery, the idea of symmetry protected topological states is generalized to other systems, leading to different topological states, including topological crystalline insulators[3–7] that are protected by crystalline symmetry, topological superconductors[8–11] which require particle-hole symmetry, and topolgical semimetals (TSMs)[12–25]. Most current experimental studies of topological states are focused on non-magnetic materials that preserve time reversal symmetry[26] and ferromagnetic materials (mainly the quantum anomalous Hall effect)[27–30]. Theoretically, a large variety of topological states can also exist in materials with other types of magnetic structures, such as anti-ferromagnetism (AFM)[31–37]. Nevertheless, material proposals of these topological states are still rare.

Half-Heusler compounds are a large group of materials consisting of three metal elements and have been widely studied for their flexible electronic properties and functionalities[38]. Around 50 half-Heusler compounds are theoretically predicted to possess inverted band structure and can be driven into the topological insulating phase by applying strains[39–43]. Unusual surface states were recently observed experimentally in LnPtBi(Ln=Lu, Y)[44] and LuPtSb[45], and serve as an evidence of non-trivial bulk topology. Weyl semimetal (WSM) phase was theoretically discussed in several half-Heusler compounds, including GdPtBi under external magnetic fields[46] and LaPtBi with in-plane strain[47], and the corresponding evidences were found in recent experiments[48–50]. Our interest in this work is focused on possible topological states in half-Heusler materials with AFM at zero external magnetic field. AFM has been experimentally observed in RPdBi (R = Er, Ho, Gd, Dy, Tb, Nd) and GdPtBi[51–57], with Neel temperature ranging from 1K to 13K. To describe AFM in half-Heusler compounds, we construct a generalized six-band Kane model with anti-ferromagnetic coupling terms based on the symmetry principle and justify this model with the microscopic tight-binding model. With this model, we predicted a large variety of time reversal breaking TSM phases, including Dirac semimetal (DSM) phase (if inversion symmetry breaking is insignificant), WSM phase, nodal line semimetal (NLSM) phase (if AFM preserves mirror or glide symmetry) and Type-B triple point semimetal (TPSM) phase[58] (if AFM preserves C_3 and glide symmetries), and topological insulating phases, including topological mirror (or glide) insulating (TMI) phase and anti-ferromagnetic topological insulating (AFMTI) phase that is protected by the combination of time reversal and half translation, depending on the material parameters. We also discuss phase diagrams of this model and identify the candidate half-Heulser compounds to search for these topological phases experimentally.

This paper is organized as follows. In Sec.II, we first present our generalized six-band Kane model and describe the symmetry aspect of this model. In Sec.III, we focus on the 4×4 block of this model which is relatively simple and includes all the four Γ_8 bands that are close to Fermi energy. A variety of topological phases, including DSM phase, WSM phase, NLSM phase, type-B TPSM phase and TMI phase, were identified for different aligning direction of magnetic moments of AFM. In Sec.IV, we discuss the limitation of the four-band model and extract the phase diagram of the six-band Kane model. We demonstrate a robust realization of AFMTI phase in half-Heusler materials with AFM once anti-ferromagnetic coupling is strong enough. The conclusion is drawn in Sec.V.

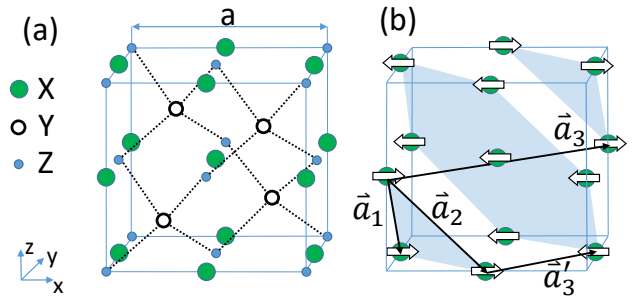

FIG. 1. (a)Crystal structure of half-Heusler alloy XYZ. (b) The alignment of magnetic moments at X atoms is shown schematically by arrows. Magnetic moments align ferromagnetically in one layer perpendicular to (111) direction and anti-ferromagnetically between two adjacent layers (type-G anti-ferromagnetic ordering). $\mathbf{a}_1$, $\mathbf{a}_2$ and $\mathbf{a}_3$ label three lattice basis vectors of the lattice with AFM, whereas $\mathbf{a}_1$, $\mathbf{a}_2$ and $\mathbf{a}'_3$ are the original lattice basis vectors of FCC lattice without AFM.

II. Model Hamiltonian of Anti-ferromagnetic Half-Heusler Materials

We start with a derivation of the model Hamiltonian for half-Heusler materials with AFM. The half-Heusler compound is normally labelled by XYZ[59], in which two metal atoms X and Y together play the role of cations and the metal atom Z is regarded as anions. The crystal structure of half-Heusler materials is shown in Fig.1a, in which X and Z atoms form the NaCl-type substructure and Y and Z atoms form the zinc-blende substructure. For certain half-Heusler materials with AFM, including GdPtBi, DyPdBi, HoPdBi and TbPdBi[53,55,56], magnetic moments come from the X atom and align ferromagnetically in one layer perpendicular to (111) direction and anti-ferromagnetically between two adjacent layers (type-G anti-ferromagnetic ordering), as shown in Fig.1b, while the exact direction of magnetic moments is still not clear and may depend on detailed compound composition.

To construct the effective Hamiltonian, we need to understand the symmetry aspect of this crystal. Without magnetic moments, the space group of half-Heusler compounds is $F\bar{4}3m$[59] and the corresponding point group is T_d, similar to zinc-blende structure. As a result, the lattice vectors should be chosen to be those of a face-centered cubic lattice, labelled as $\mathbf{a}_1$, $\mathbf{a}_2$ and $\mathbf{a}'_3$ in Fig.1b. The existence of type-G AFM has two main effects to the symmetry of the system: (1) it doubles the lattice vector and the unit-cell along the $\mathbf{a}'_3$ direction, and the new lattice vector is labeled as $\mathbf{a}_3 = 2\mathbf{a}'_3$; (2) in the mean field level, the magnetic moments of AFM give rise to exchange coupling to electron spins. Due to the doubling of unit-cell, the space group and point group of the crystalline structure are reduced to $R3m$[60] and C_{3v}, where the latter has two generators: three-fold rotation $C_3(111)$ along (111) direction and mirror symmetry $\pi_{(1\bar{1}0)}$ with respect to $(1\bar{1}0)$ plane. As a pseudo-vector, magnetic moments of AFM can further lower the symmetry. Besides the above crystal symmetries, another essential symmetry due to AFM is the combination of time reversal Θ and half tranlation $T_{\mathbf{a}'_3}$, denoted as $S \equiv T_{\mathbf{a}'_3}\Theta$.

Similar to the semiconductors with the zinc-blende structure, the low energy physics of half-Heusler materials can be described by two Γ_6 bands with s-orbital nature, labelled by $|\Gamma_6, S_z\rangle$ with z-directional spin component $S_z = \pm\frac{1}{2}$, and four Γ_8 bands with p-orbital nature, labelled by $|\Gamma_8, J_z\rangle$ with total angular momentum $J_z = \pm\frac{1}{2}, \pm\frac{3}{2}$ which is a combination of spin and orbital angular momentum. Here the notations Γ_6 and Γ_8 refer to the irreducible representations of the corresponding bands under the T_d group[61] and we still keep this notation even though the symmetry is lowered. The form and symmetry of the basis wave functions are also justified with microscopic local atomic orbitals, as discussed in details in Appendix A. It should be emphasized that due to the doubling of the unit-cell, the basis wave functions in the new unit-cell is a bonding or anti-bonding state of the basis functions in the original unit-cell. For the low energy physics, we find both $|\Gamma_6, S_z\rangle$ and $|\Gamma_8, J_z\rangle$ are bonding states in the doubled unit-cell and are still suitable to be bases. To obtain a matrix expansion of the effective Hamiltonian, we need to classify all the matrices according to the irreducible representations of the symmetry group for the above basis. The Hamiltonian should be invariant under symmetry operations of the symmetry group, which means it belongs to the identity representation, and can be constructed by combining the symmetrized matrices and symmetrized tensor components of physical quantities (such as the momentum $\mathbf{k}$ and the order parameters $\mathbf{M}$ for AFM) which belong to the same irreducible representation.[61] This symmetry approach allows us to systematically construct the full Hamiltonian, including the standard six-band Kane model and an additional AFM term. The standard six-band Kane model is[61]

$$H_{Kane} = \left(\begin{array}{c|c} H_{\Gamma_6}(\mathbf{k}) & V \\ \hline V^\dagger & H_{\Gamma_8}(\mathbf{k}) \end{array}\right), \tag{1}$$

where

$$\begin{aligned} V = & \frac{P}{\sqrt{6}}\begin{pmatrix} -\sqrt{3}k_+ & 2k_z & k_- & 0 \\ 0 & -k_+ & 2k_z & \sqrt{3}k_- \end{pmatrix} \\ & + \frac{B^+_{8v}}{\sqrt{6}}\begin{pmatrix} \sqrt{3}k_-k_z & 2ik_xk_y & k_+k_z & 0 \\ 0 & k_-k_z & 2ik_xk_y & \sqrt{3}k_+k_z \end{pmatrix} \\ & + \frac{B^-_{8v}}{3\sqrt{2}}\begin{pmatrix} 0 & \sqrt{3}K^2 & 0 & k_\parallel^2 - 2k_z^2 \\ -k_\parallel^2 + 2k_z^2 & 0 & -\sqrt{3}K^2 & 0 \end{pmatrix} \end{aligned}, \tag{2}$$

$$H_{\Gamma_6}(\mathbf{k}) = (E_c + \beta_c k^2)\mathbb{1}_2 \tag{3}$$

with $\mathbb{1}_2$ to be the 2×2 identity matrix,

$$H_{\Gamma_8}(\mathbf{k}) = H_0(\mathbf{k}) + H_C(\mathbf{k}) \tag{4}$$

ξ_0	$\alpha_1(M_x^2+M_y^2+M_z^2)+\beta_1(M_yM_z+M_zM_x+M_xM_y)$
ξ_1	$\alpha_3(2M_z^2-M_x^2-M_y^2)+\beta_3(2M_xM_y-M_yM_z-M_zM_x)$
ξ_2	$\alpha_3\sqrt{3}(M_x^2-M_y^2)+\beta_3\sqrt{3}(M_yM_z-M_xM_z)$
ξ_3	$\alpha_2(M_x^2+M_y^2+M_z^2)+\beta_2(M_yM_z+M_zM_x+M_xM_y)$ $+2[\alpha_4(2M_z^2-M_x^2-M_y^2)+\beta_4(2M_xM_y-M_yM_z-M_zM_x)]$
ξ_4	$\alpha_2(M_x^2+M_y^2+M_z^2)+\beta_2(M_yM_z+M_zM_x+M_xM_y)$ $-[\alpha_4(2M_z^2-M_x^2-M_y^2)+\beta_4(2M_xM_y-M_yM_z-M_zM_x)]$ $-\sqrt{3}[\alpha_4\sqrt{3}(M_x^2-M_y^2)+\beta_4\sqrt{3}(M_yM_z-M_xM_z)]$
ξ_5	$\alpha_2(M_x^2+M_y^2+M_z^2)+\beta_2(M_yM_z+M_zM_x+M_xM_y)$ $-[\alpha_4(2M_z^2-M_x^2-M_y^2)+\beta_4(2M_xM_y-M_yM_z-M_zM_x)]$ $+\sqrt{3}[\alpha_4\sqrt{3}(M_x^2-M_y^2)+\beta_4\sqrt{3}(M_yM_z-M_xM_z)]$

TABLE I. Expressions for the ξ_i parameters ($i=0,1,2,3,4,5$) in the AFM Hamiltonian (Eq.7). Here M_i's are three components of the anti-ferromagnetic magnetic moment, and α_i's, β_j's are parameters independent of each other and momentum $\mathbf{k}$.

with

$$H_0(\mathbf{k})=\tfrac{4}{15}(J_x^2+J_y^2+J_z^2)h_0+\tfrac{1}{3}(2J_z^2-J_x^2-J_y^2)h_1 +\tfrac{1}{\sqrt{3}}(J_x^2-J_y^2)h_2+\tfrac{2}{\sqrt{3}}J_{xy}h_3+\tfrac{2}{\sqrt{3}}J_{zx}h_4+\tfrac{2}{\sqrt{3}}J_{yz}h_5 \tag{5}$$

and

$$H_C(\mathbf{k})=\frac{2}{\sqrt{3}}C(k_xV_x+k_yV_y+k_zV_z). \tag{6}$$

Here we have $h_0=E_v-\beta_c\gamma_1k^2$, $h_1=\beta_c\gamma_2(2k_z^2-k_\parallel^2)$, $h_2=\sqrt{3}\beta_c\gamma_2K^2$, $h_3=2\sqrt{3}\beta_c\gamma_3k_xk_y$, $h_4=2\sqrt{3}\beta_c\gamma_3k_xk_z$, and $h_5=2\sqrt{3}\beta_c\gamma_3k_yk_z$. J_i's are angular momentum matrices for spin 3/2 (see Appendix B for details), $J_{ij}=\frac{1}{2}\{J_i,J_j\}$, $V_x=\frac{1}{2}\{J_x,J_y^2-J_z^2\}$, $V_y=\frac{1}{2}\{J_y,J_z^2-J_x^2\}$, $V_z=\frac{1}{2}\{J_z,J_x^2-J_y^2\}$, $\beta_c=\hbar^2/(2m')$, m' is the effective mass of Γ_6 bands near Γ point, $k^2=k_x^2+k_y^2+k_z^2$, $k_\parallel^2=k_x^2+k_y^2$, $K^2=k_x^2-k_y^2$ and $k_\pm=k_x\pm ik_y$. In this work, $\beta_c>0$, $\gamma_2\neq0$ and $\gamma_3\neq0$ are always assumed, unless being specified otherwise. Besides the above terms in the standard Kane model, AFM can lead to new terms, which can be constructed in a similar manner with the symmetry group combining point group C_{3v}, $T_{\mathbf{a}_3'}$ and Θ (see Appendix B for more details). For the materials that we are interested in, the main influence of AFM only occurs for the four Γ_8 bands. Thus, we only consider the anti-ferromagnetic terms in the basis of the four Γ_8 bands and the corresponding Hamiltonian is given by

$$H_{AFM}=\tfrac{4}{15}(J_x^2+J_y^2+J_z^2)\xi_0+\tfrac{1}{3}(2J_z^2-J_x^2-J_y^2)\xi_1 +\tfrac{1}{\sqrt{3}}(J_x^2-J_y^2)\xi_2+\tfrac{2}{\sqrt{3}}J_{xy}\xi_3+\tfrac{2}{\sqrt{3}}J_{zx}\xi_4+\tfrac{2}{\sqrt{3}}J_{yz}\xi_5, \tag{7}$$

where the detailed expressions for ξ_i ($i=0,\ldots,5$) are listed in Tab.I.

Next we discuss the symmetry properties of this Hamiltonian. For the standard Kane model H_{Kane}, if the parameter C in H_C is zero, the Hamiltonian possess O_h point group. Non-zero H_C term breaks inversion symmetry and lowers the point group from O_h to T_d. The existence of AFM results in the doubling of the unit cell along $\mathbf{a}_3'$ and reduce the point group of the lattice to C_{3v}. For a fixed non-zero anti-ferromagnetic order $\mathbf{M}$, the AFM term H_{AFM} will further reduce the symmetry. If $\mathbf{M}$ is along the (111) direction, $C_3(111)$ symmetry is maintained but all mirror symmetries in C_{3v} are broken, whereas the glide symmetries $T_{\mathbf{a}_3'}\pi_{(1\bar{1}0)}$, $T_{\mathbf{a}_3'}\pi_{(\bar{1}01)}$ and $T_{\mathbf{a}_3'}\pi_{(01\bar{1})}$ are preserved. If $\mathbf{M}$ lies in a mirror plane α ($\alpha=(1\bar{1}0)$ or $(\bar{1}01)$ or $(01\bar{1})$) but away from the (111) direction, all symmetries in C_{3v} are broken, whereas the glide symmetry $T_{\mathbf{a}_3'}\pi_\alpha$ is preserved. If $\mathbf{M}$ is perpendicular to a mirror plane of the lattice, the only remaining symmetry is that mirror symmetry. For a generic AFM Hamiltonian, $\mathbf{M}$ will break all the symmetries in C_{3v} group, as well as the combination with $T_{\mathbf{a}_3'}$. Furthermore, we notice that only quadratic terms of $\mathbf{M}$ appear in our Hamiltonian while any linear $\mathbf{M}$ terms vanish. This is because $\mathbf{M}$ reverses its sign under translation $T_{\mathbf{a}_3'}$, while translation $T_{\mathbf{a}_3'}$ is just identity matrix for the basis of four Γ_8 bands and thus commutes with any representation matrix (see Appendix B for more details). This suggests that any term with the odd orders of the anti-ferromagnetic order parameter $\mathbf{M}$ cannot exist.

III. Topological Phases in the Four-band Model

Since we are interested in the half-Heusler materials with inverted band structures, only four Γ_8 bands appear near the Fermi energy while the Γ_6 bands are far below the Fermi energy. Thus, we first focus on the four Γ_8 bands with the Hamitonian $H_{\Gamma_8}(\mathbf{k})+H_{AFM}$. For the inverted band structure, the Fermi energy is between the Γ_8 bands, and the two Γ_8 bands with lower energies are valence bands while the other two Γ_8 bands with higher energies are conduction bands. We emphasize that the Γ_6 bands are important for certain types of topological states even though they are away from the Fermi energy, as discussed in details in the next section. However, for the TSM phases discussed in this section, only the Γ_8 bands are essential. Another advantage of the 4-band Hamiltonian is that it can be solved analytically in certain limit, thus providing us valuable insight into the underlying physics. In this section, we first focus on the case without inversion symmetry breaking term (i.e. choosing $H_C(\mathbf{k})=0$) and reveal the occurence of DSM phase due to the coexistence of inversion symmetry and anti-unitary S symmetry. In realistic system, inversion symmetry is broken and DSM phase becomes unstable. Nevertheless, DSM phase can be viewed as the "parent" phase to generate other TSM phases after including $H_C(\mathbf{k})$. We further study the situation with non-zero inversion symmetry breaking term $H_C(\mathbf{k})$, focusing on the situations with (1) magnetic moments polarized within or perpendicular to the $(1\bar{1}0)$ plane and (2) $\mathbf{M}$ along the (111) direction.

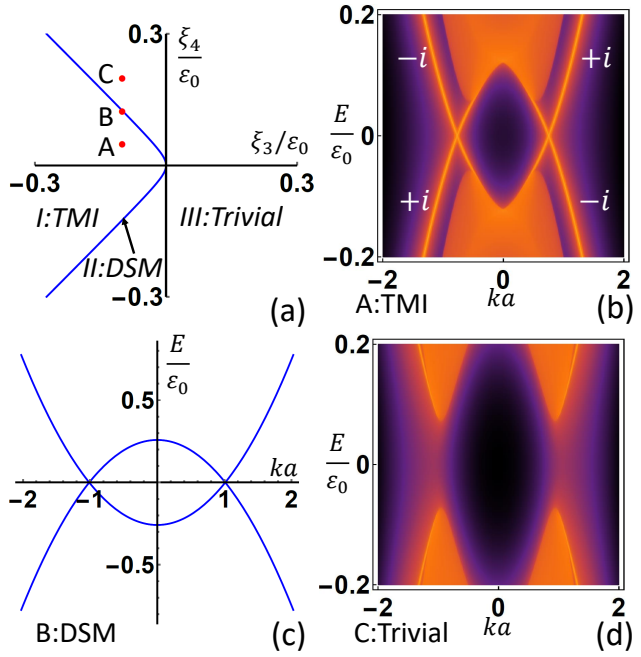

FIG. 2. (a) Phase Diagram as a function of ξ_3 and ξ_4 for the Hamiltonian $H_0(\mathbf{k})+H_{AFM}$. Here phase I is TMI phase, phase III is trivial insulating phase, and phase II is DSM phase that serves as a critical line separating phase I and III. (b) reveals the local density of states on (001) surface for point A in (a) with $(\xi_3,\xi_4)=(-0.1,0.05)\varepsilon_0$, which is in TMI phase. k is along (110) direction. $\pm i$ are mirror eigenvalues of corresponding bands. (c) Energy spectrum for the point B in (a), which is in DSM phase. k is along the line connecting two Dirac points and each band is doubly degenerated. (d) reveals the local density of states on (001) surface for point C in (a) with $(\xi_3,\xi_4)=(-0.1,0.2)\varepsilon_0$, which is in the trivial insulating phase. k is along (110) direction.

A. Dirac Semimetal Phase and Topological Mirror Insulating Phase

In this part, $H_C(\mathbf{k})=0$ is assumed and the total Hamiltonian takes the form $H_0(\mathbf{k})+H_{AFM}$ with inversion symmetry. In this case, the eigenenergy of Hamiltonian can be solved analytically as

$$E_{0+AFM,\pm}(\mathbf{k})=(h_0+\xi_0)\pm\sqrt{\sum_{i=1}^{5}(h_i+\xi_i)^2}. \quad (8)$$

Without AFM term, $\xi_i=0$ for $i=0,\ldots,5$ in Eq.7, and there are four-fold degeneracy of the Γ_8 bands at the Γ point ($\mathbf{k}=0$) due to the T_d group symmetry. The conduction and valence bands touch each other quadratically at $\mathbf{k}=0$, leading to a critical semimetal phase for the four-band Luttinger model $H_0(\mathbf{k})$. Early studies have demonstrated various TSM phases induced by strain or external magnetic fields in this system[47,49]. The AFM term H_{AFM} can lower the symmetry of the system and remove the four-fold degeneracy at Γ point. However, since H_{AFM} preserves the inversion symmetry and S symmetry, all the bands are still doubly degenerate, similar to the Kramer's degeneracy due to inversion and time reversal symmetries[62].

Next we will study the influence of AFM term on the energy dispersion. The AFM term can lead to a non-zero gap at Γ point, given by $2\sqrt{\xi_1^2+\xi_2^2+\xi_3^2+\xi_4^2+\xi_5^2}$. Thus, the two doubly degenerate bands are split at the Γ point, but they may cross each other at some finite momenta $\mathbf{k}$, giving rise to a semimetal phase. The realization of such semimetal phase requires $h_i+\xi_i=0$ for all $i=1,\ldots,5$ and the details are discussed in Appendix C. Here we focus on the cases where magnetic moments of AFM are perpendicular to $(1\bar{1}0)$ plane ($M_x=-M_y$ and $M_z=0$, where $M_{x,y,z}$ are x,y,z components of AFM magnetic moment $\mathbf{M}$) with mirror symmetry $\pi_{(1\bar{1}0)}$, or lie in the $(1\bar{1}0)$ plane ($M_x=M_y$) with the glide symmetry $T_{\mathbf{a}_3'}\pi_{(1\bar{1}0)}$. According to the expressions of ξ_i's, both conditions imply the same requirement for parameters: $\xi_2=0$ and $\xi_4=\xi_5$, which is reasonable since $\pi_{(1\bar{1}0)}$ and $T_{\mathbf{a}_3'}\pi_{(1\bar{1}0)}$ have the same matrix representation for four basis wave functions of Γ_8 bands. For the existence of gapless points, one of the following additional conditions is required for the values of ξ_1, ξ_3 and ξ_4 (see Appendix C for more details): (i) $\xi_3\beta_c\gamma_3<0$, $\sqrt{3}\gamma_3\xi_3\xi_1+\gamma_2\left(\xi_3^2-\xi_4^2\right)=0$; (ii) $\xi_3=\xi_4=0$, $\xi_1\beta_c\gamma_2<0$; (iii) $\xi_4=0$, $\xi_3\beta_c\gamma_3>0$, $\sqrt{3}\gamma_3\xi_1-\gamma_2\xi_3=0$. Due to $\xi_2=0$ and $\xi_4=\xi_5$, we require $k_x^2=k_y^2$ and $k_xk_z=k_yk_z$ from $h_i=-\xi_i$ with $i=2,4,5$, indicating two possibilities for the locations of gapless point, either on the plane $(1\bar{1}0)$ with the form (k_1,k_1,k_3) for the conditions (i) and (ii), or on the $(1,-1,0)$ axis with the form $(k_1,-k_1,0)$ for the condition (iii). Due to the S symmetry, if a gapless point occurs at a finite momentum $\mathbf{k}_0$, there must be another one at $-\mathbf{k}_0$, leading to even number of gapless points. The number of gapless points are confirmed to be 2 by solving for positions of gapless points in each case (see Appendix C for more details).

Based on the above conditions for gapless points, we can further extract the phase diagram of this model as a function of (ξ_3,ξ_4). An example of a phase diagram is shown in Fig.2a for the choices of parameters listed in Tab.VI in Appendix F. The blue line in the phase diagram, labelled by II, represents DSM phase. For our choices of the parameters, the condition (i) or (ii) can be satisfied and Dirac points are on the $(1\bar{1}0)$ plane. Fig.2c reveals a typical energy dispersion of the semimetal phase at the point B in Fig.2a with $\xi_3/\varepsilon_0=-\frac{1}{10}$ and $\xi_4/\varepsilon_0=\frac{1}{50}\sqrt{8\sqrt{3}+25}$ to satisfy the condition (i), where the energy unit ε_0 is defined as $\varepsilon_0\equiv\beta_c/a^2$ and a is a real positive parameter with unit of length. The energy dispersion around the gapless point behaves linearly, thus forming two Dirac cones at $\mathbf{k}a=\pm\frac{1}{\sqrt[4]{12}}(1,1,-\frac{1}{5}\sqrt{8\sqrt{3}+25})$, given the double degeneracy for each band. Further theoretical analysis of the effective low-energy Hamiltonian expanded around these two gapless points confirms this DSM phase, as shown in details in Appendix D.

The DSM phase separates two insulating phases, la-

beled by I and III in Fig.2a. To identify the nature of these two insulating phases, we perform a numerical calculation of energy dispersion on the (001) surface of an approximately semi-infinite sample.[63] The local density of states at the top surface along $k_x = k_y$ axis is shown in Fig.2b for the point A with $(\xi_3, \xi_4) = (-0.1, 0.05)\varepsilon_0$ in the phase I and Fig.2d for the point C with $(\xi_3, \xi_4) = (-0.1, 0.2)\varepsilon_0$ in the phase III, respectively. One can see two sets of gapless modes appearing for the phase I while a full gap existing for the phase III. Thus, we expect the phase I is topologically non-trivial while the phase III is trivial. We also perform a calculation of mirror Chern number (MCN)[64] on the mirror or glide plane $(1\bar{1}0)$ for this system and find MCN to be 2 for the phase I and 0 for the phase III. This confirms that two sets of gapless modes in Fig.2b are protected by mirror or glide symmetry and makes phase I to be TMI phase. Thus, DSM phase can be viewed as the topological phase transition point between a TMI phase and a trivial insulating phase.

We emphasize that, in realistic half-Heusler materials, inversion symmetry is absent and the Kramer's degeneracy at a generic $\mathbf{k}$ is split for both the conduction and valence bands, which means Dirac points are also split. However, DSM phase will evolve into other TSM phases, as discussed in the next section. Therefore, DSM phase can be viewed as the "parent" phase to search for and understand other topological phases.

B. Weyl Semimetal Phase and Topological Mirror Insulating Phase

In this part, we include the inversion symmetry breaking term $H_C(\mathbf{k})$ into the four-band Hamiltonian and the total Hamiltonian becomes $H_{\Gamma_8}(\mathbf{k}) + H_{AFM}$. As a consequence, the Kramer's degeneracy of each band at a generic momentum $\mathbf{k}$ is split. We still consider the magnetic moments of anti-ferromagnetic ordering aligning within or perpendicular to the $(1\bar{1}0)$ plane to preserve either the glide symmetry $T_{\mathbf{a}_3'}\pi_{(1\bar{1}0)}$ or the mirror symmetry $\pi_{(1\bar{1}0)}$, which gives $\xi_2 = 0$ and $\xi_4 = \xi_5$. Due to the existence of H_C term, the full Hamiltonian cannot be diagonalized analytically and thus numerical methods are adopted to extract phase diagram. All the parameters are the same as previous choices, except the C parameter which is chosen as $C = 0.2(\beta_c/a)$, as listed in Tab.VII in Appendix F.

The phase diagram as a function of ξ_3 and ξ_4 is shown in Fig.3a. The phases I and III in Fig.3a remain robust due to existence of mirror or glide symmetry. A direct calculation of surface local density of states, as well as MCN, shows four surface modes with MCN being 2 (Fig.3c) for point A in Fig.3a ($\xi_3/\varepsilon_0 = -0.2$ and $\xi_4/\varepsilon_0 = 0.01$) and a full gap with zero MCN (Fig.3d) for point C in Fig.3a ($\xi_3/\varepsilon_0 = 0.3$ and $\xi_4/\varepsilon_0 = 0.1$).

We notice that the phase II is expanded from a line of Dirac semimetal phase in Fig.2a to a region of WSM phase in Fig.3a. The reason is that H_C breaks the inversion symmetry and splits each Dirac cone in Dirac semimetal phase into two Weyl points. Since there are two Dirac points in the DSM phase, the phase II in Fig.3a typically has four Weyl points in the whole momentum space, denoted as $\mathbf{K}_i$ $(i = 1, 2, 3, 4)$, as shown in Fig.3b and Fig.4a. Different Weyl points can be related to each other by symmetries: $\mathbf{K}_1$ and $\mathbf{K}_2$ (or $\mathbf{K}_3$ and $\mathbf{K}_4$) are related by $\Pi_{(1\bar{1}0)} \equiv \pi_{(1\bar{1}0)}$ or $T_{\mathbf{a}_3'}\pi_{(1\bar{1}0)}$ and therefore dubbed a 'Π pair', $\mathbf{K}_1$ and $\mathbf{K}_3$ (or $\mathbf{K}_2$ and $\mathbf{K}_4$) are related by $\Pi_{(1\bar{1}0)}S$ and called a 'ΠS pair', and finally $\mathbf{K}_1$ and $\mathbf{K}_4$ (or $\mathbf{K}_2$ and $\mathbf{K}_3$) are related by S and named a 'S pair'. It is known[65–67] that a Weyl fermion can carry topological charge or chirality, which can be extracted from Chern number (CN) on a small spherical surface surrounding the Weyl point. Two Weyl points related by mirror symmetry have opposite Chern numbers while time reversal operation leaves Chern number of a Weyl point unchanged. As a result, a Π pair carries opposite CNs and so does a ΠS pair, while a S pair has the same CN. Due to the existence of topological charge, a single

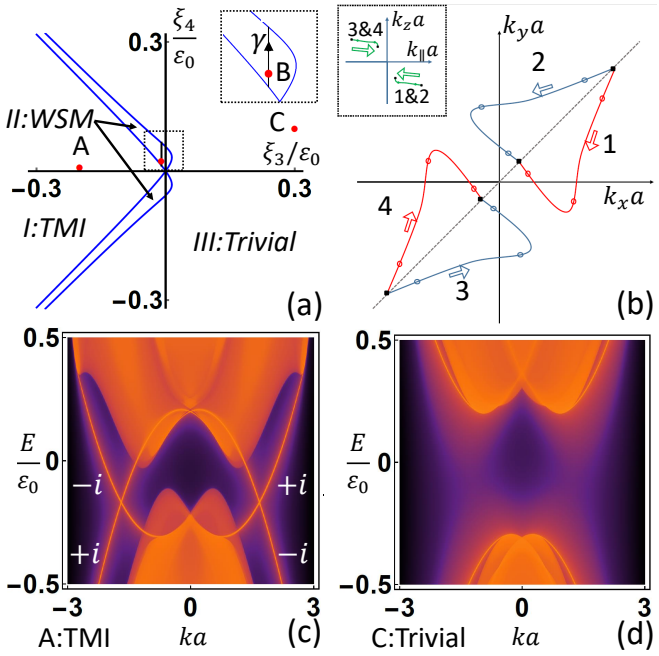

FIG. 3. (a)Phase Diagram as a function of ξ_3 and ξ_4, in which the phase I is a topological mirror insulator, the phase III is a trivial insulator, and the phase II is a Weyl semi-metal phase. The determination of boundary of phase II is described in Appendix G. The inset is a zoom-in version for the boxed part of phase II. (b) is a schematic for the motion of Weyl points along the path γ in the inset of (a). The main graph shows the projection of the motion on the $k_x - k_y$ plane, and the inset depicts the projection of the motion on $(1\bar{1}0)$ plane which is the mirror or glide plane. (c) and (d) reveal the local density of states on (001) surface for point A ($\xi_3/\varepsilon_0 = -0.2$ and $\xi_4/\varepsilon_0 = 0.01$) and C ($\xi_3/\varepsilon_0 = 0.3$ and $\xi_4/\varepsilon_0 = 0.1$) in (a) respectively. k is chosen to be along (110) direction. $\pm i$ in (c) are mirror eigenvalues of corresponding bands. A is in TMI phase while C is in trivial insulating phase.

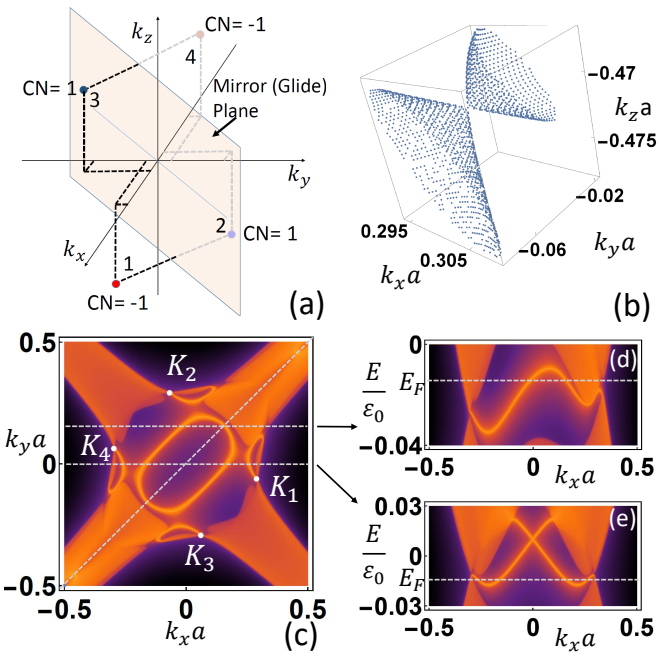

FIG. 4. This figure is for point B in Fig.3a with $\xi_3 = -0.01\varepsilon_0$ and $\xi_4 = 0.025\varepsilon_0$. (a) shows schematically the positions of four Weyl points with the corresponding CNs. (b)The Fermi surface around Weyl point $\mathbf{K}_1$ shows that it is a type-II Weyl point. (c)Local density of states on (001) surface at the energy of Weyl points (Fermi energy). Weyl points are represented by white dots and connected to Fermi arcs. Two horizontal grey dashed lines correspond to the momentum line $k_y a = 0$ and $k_y a = 0.15$. The grey dashed line along the diagonal direction corresponds to the momentum line $k_x = k_y$ with mirror or glide symmetry. (d) and (e) depict local density of states on (001) surface along the momentum line $k_y a = 0.15$ and $k_y a = 0$ respectively, and the horizontal lines inside them mark the chosen Fermi energy (energy of Weyl points).

Weyl point cannot be gapped and it can only move in the momentum space when tuning the parameters until it merges with another Weyl point with opposite CN. We track the motion of Weyl points through the path γ in the inset of Fig.3a, and find $\mathbf{K}_1$ and $\mathbf{K}_2$ (or $\mathbf{K}_3$ and $\mathbf{K}_4$) emerge from a point in the mirror (or glide) plane as a II pair and move in the momentum space and finally annihilate at another point on the mirror (or glide) plane, as shown in Fig.3b with its inset.

Now we focus on the energy dispersion of the WSM phase by choosing the B point in Fig.3a with $\xi_3 = -0.01\varepsilon_0$ and $\xi_4 = 0.025\varepsilon_0$ as an example. Four Weyl points are approximately located at

$$\begin{aligned}\mathbf{K}_1 a &= \{0.30, -0.047, -0.47\},\\ \mathbf{K}_2 a &= \{-0.047, 0.30, -0.47\},\\ \mathbf{K}_3 a &= \{0.047, -0.30, 0.47\},\\ \mathbf{K}_4 a &= \{-0.30, 0.047, 0.47\}\end{aligned}$$

in the momentum space, respectively. By integrating the Berry curvature on the sphere around each point, we found CNs of four Weyl points are $CN_1 = -1, CN_2 = 1, CN_3 = 1$ and $CN_4 = -1$ (see Fig.4a), which is consistent with the symmetry analysis above. The Fermi surface around $\mathbf{K}_1$ at the energy of the Weyl point, as shown in Fig.4b, demonstrates the existence of a type II Weyl point[19,20] in our system. Type-II Weyl fermions are topologically non-trivial and can lead to Fermi arc[20] on the surface. Thus, we perform a calculation of local density of states at the energy of Weyl points on the (001) surface of an approximately semi-infinite sample[63], as shown in Fig.4c, in which a complex surface Fermi arcs overlaps with bulk bands. Weyl points are depicted by white points in the plot and there is one Fermi arc starting from each Weyl point and merging into bulk bands. Additional surface states with same energy exist and they form a circle surrounding the Γ point $\mathbf{k} = 0$. The surface energy dispersions along the momentum lines $k_y a = 0$ and $k_y a = 0.15$ are shown in Fig.4d and Fig.4e. We notice one chiral edge mode existing along the momentum line $k_y a = 0.15$ while a helical edge mode along the line $k_y a = 0$. We may treat k_y as a parameter and consider two-dimensional (2D) planes formed by k_z and k_x for different k_y. According to the bulk-edge correspondence, the existence of chiral edge mode for $k_y a = 0.15$ at the surface suggests $CN = -1$ for the corresponding 2D plane. Similarly, CN for the 2D plane at $k_y a = 0$ should be zero. This is consistent with the fact that two 2D planes at $k_y a = 0.15$ and $k_y a = 0$ enclose one Weyl point $\mathbf{K}_4$ whose CN is -1. However, the helical edge mode along the line $k_y a = 0$ cannot be explained by CN. The crossing point between two branches of the helical edge mode is protected by S symmetry, thus the 2D plane at $k_y a = 0$ can be viewed as an AFMTI phase. In addition, since the crossing point at $\mathbf{k} = 0$ also falls into the mirror (or glide) plane, as shown by diagonal line in Fig.4c, that crossing point thus can also be protected by MCN, which is equal to 1 for the phase II. Therefore, two blue lines in Fig.3a can be viewed as transition lines between the phase II with $MCN = 1$ and the phase I or III with MCN being 0 or 2 respectively.

Although we focus on the magnetic moments parallel or perpendicular to the mirror plane in this section, the WSM phase can NOT be destroyed immediately when magnetic moments is tilted away from these directions due to the non-zero CNs carried by Weyl points. The Weyl points can only move in the momentum space and should be robust in certain parameter regimes. On the other hand, for the TMI phase, gapless points of helical surface mode at finite non-zero momenta are solely protected by the mirror or glide symmetry and thus sensitively depend on the direction of magnetic moments.

C. Nodal Line Semimetal Phase

For magnetic moments of anti-ferromagnetic ordering within or perpendicular to the $(1\bar{1}0)$ plane, another possible TSM phase is NLSM phase. An example of NLSM phase is shown in Fig.5, where the parameters are shown

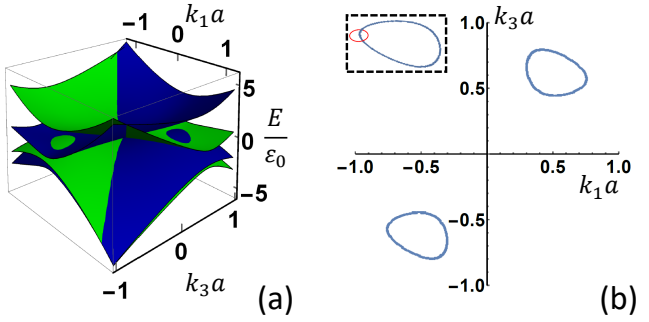

FIG. 5. (a)Energy dispersion on $(1\bar{1}0)$ plane with green and blue bands coming from $+i$ and $-i$ mirror subspace, respectively. Here $k_{1,2,3}$ are defined as $(k_x, k_y, k_z) = (\frac{k_1}{\sqrt{6}} - \frac{k_2}{\sqrt{2}} + \frac{k_3}{\sqrt{3}}, \frac{k_1}{\sqrt{6}} + \frac{k_2}{\sqrt{2}} + \frac{k_3}{\sqrt{3}}, -\frac{2k_1}{\sqrt{6}} + \frac{k_3}{\sqrt{3}})$. (b)The positions of nodal rings on $(1\bar{1}0)$ plane. The inset shows that the red circle around the nodal ring , along which accumulated Berry phase is π.

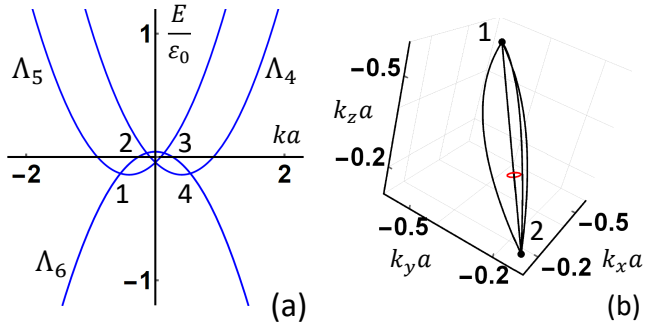

FIG. 6. (a)Band dispersion along the (111) direction for TPSM phase. Λ_4 and Λ_5 label two different non-degenerate bands whereas Λ_6 labels a doubly degenerate band. The crossing points 1,2,3,4 are triple points with three-fold degeneracy. (b) Black dots denote the positions for the points 1 and 2 in the momentum space and are conntected by four nodal lines (black lines). Berry phase accumulated along the red circle around any nodal line is π.

in Tab.VIII in Appendix F. Due to differnet AFM parameters, the band sequence is different and two crossing bands at the low energy are from two opposite mirror subspaces, in contrast to the band crossing between two bands with the same mirror parity for the phase boundary in Fig.3a. The energy dispersion of NLSM phase is depicted in Fig.5a and the positions of two nodal rings are shown in Fig.5b. The topological stability of each nodal ring can be extracted by the π Berry phase along a small circle (red circle in inset of Fig.5b) around the nodal line. Topological characterization of such mirror symmetry protected nodal ring has been well studied in Ref.[68].

D. Triple Point Semimetal Phase

In this section, we consider the case with antiferromagnetic magnetic moments along the (111) direction, where the system has three-fold rotational symmetry $C_3(111)$ and glide symmetry $T_{\mathbf{a}_3'}\pi_{(1\bar{1}0)}$. Since the matrix representation of $T_{\mathbf{a}_3'}\pi_{(1\bar{1}0)}$ is equivalent to the mirror symmetry $\pi_{(1\bar{1}0)}$ for the basis of Γ_8 bands, the symmetry group generated by $C_3(111)$ and $T_{\mathbf{a}_3'}\pi_{(1\bar{1}0)}$ is isomorphic to the point group C_{3v}. By linearly combining the four basis functions of Γ_8 bands which carry total angular momentum $J = \frac{3}{2}$, we can get a pair of states belonging to two-dimensional representation Λ_6 of the C_{3v} double group, and the other two states belonging to two one-dimensional representations Λ_4 and Λ_5 respectively.[69] The character table of the C_{3v} double group and the linear combinations of Γ_8 bases are shown in Appendix E.

To confirm this symmetry analysis, we consider the total Hamiltonian $H_0(\mathbf{k}) + H_C(\mathbf{k}) + H_{AFM}$ with magnetic moments along the (111) direction ($M_x = M_y = M_z$). This corresponds to the conditions $\xi_1 = \xi_2 = 0$ and $\xi_3 = \xi_4 = \xi_5$. Along the (111) direction, we indeed find that four Γ_8 bands are split into one doubly degenerate band, labeled as Λ_6 bands, and another two non-degenerate bands, labeled as Λ_4 and Λ_5 bands respectively. The corresponding energy dispersion can be solved analytically as

$$\begin{aligned} E_{\Lambda_6}(k) &= E_v + \xi_0 - 3\beta_c\gamma_1 k^2 - (6\beta_c\gamma_3 k^2 + \sqrt{3}\xi) \\ E_{\Lambda_5}(k) &= E_v + \xi_0 - 3\beta_c\gamma_1 k^2 + (6\beta_c\gamma_3 k^2 + \sqrt{3}\xi) + \sqrt{6}Ck \\ E_{\Lambda_4}(k) &= E_v + \xi_0 - 3\beta_c\gamma_1 k^2 + (6\beta_c\gamma_3 k^2 + \sqrt{3}\xi) - \sqrt{6}Ck \end{aligned},$$

where $\xi_3 = \xi_4 = \xi_5 \equiv \xi$ and $k_x = k_y = k_z = k$. A typical energy dispersion is shown in Fig.6a with the parameters shown in Tab.IX in Appendix F. Under the condition $C^2 > 16\sqrt{3}\beta_c\gamma_3\xi$ and $C\xi \neq 0$, the Λ_6 bands cross with the Λ_5 (Λ_4) band at two points labeled by 1 and 3 (2 and 4) in Fig.6a. At each crossing point, there is a three-fold degeneracy and the energy dispersion behave linearly along the (111) axis. Points 1 and 2 (or 3 and 4) are connected by four nodal lines, as shown in Fig.6b. Along a circle enclosing any of these four nodal lines, the accumulated Berry phase is found to be π. This type of semi-metal phase is known as type-B TPSM phase[58].

IV. Anti-ferromagnetic Topological Insulating Phase in Six-band Kane Model

In the discussion above, we neglected Γ_6 bands and only focused on four Γ_8 bands. This simplification has irrelevant influence on TSM phases since Γ_6 bands are far away from Fermi energy. However, due to the inverted nature between Γ_6 and Γ_8 bands, Γ_6 bands may play an essential role for topological insulating phases. It is well known that the band inversion between the Γ_6 and Γ_8 bands leads to the topological insulating phase in HgTe[70], as well as non-magnetic half-Heusler materials[39–42]. Therefore,we study the influence of Γ_6 bands by considering the full six-band Kane model

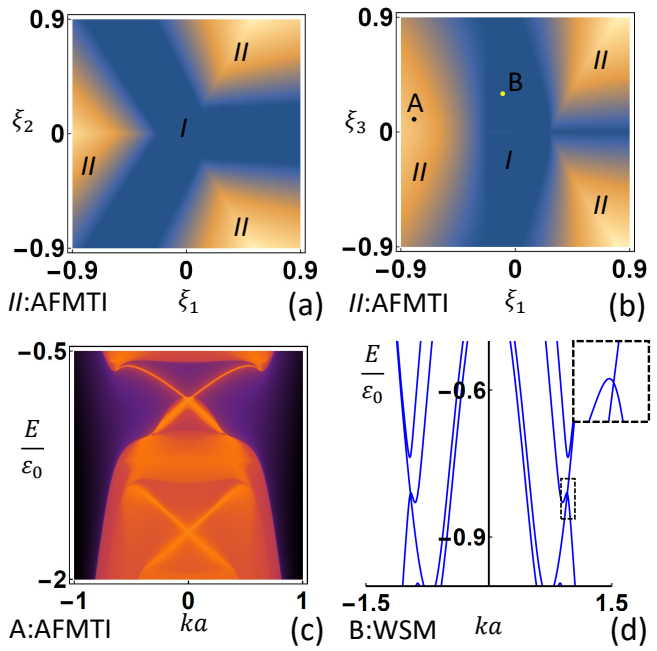

FIG. 7. The direct band gap is shown as a function of (a) ξ_1 and ξ_2 for zero $\xi_{3,4,5}$ and (b) ξ_1 and ξ_3 for zero $\xi_{2,4,5}$. Here the region I with the blue color is the TSM phase while the region II with the yellow color has non-zero direct band gap and is the AFMTI phase. (c) shows the local density of states on (001) surface for point A with $(\xi_1, \xi_3) = (-0.8, 0.1)\varepsilon_0$ in (b). k is along (110) direction. (d) shows the bulk dispersion along the line connecting two Weyl points at $\mathbf{k}a = \pm(-0.89, -0.35, 0)$. This dispersion corresponds to the point B in Fig.7b with $(\xi_1, \xi_3) = (-0.1, 0.3)\varepsilon_0$. The inset is a zoom-in plot around the momentum $\mathbf{k}a = (-0.89, -0.35, 0)$.

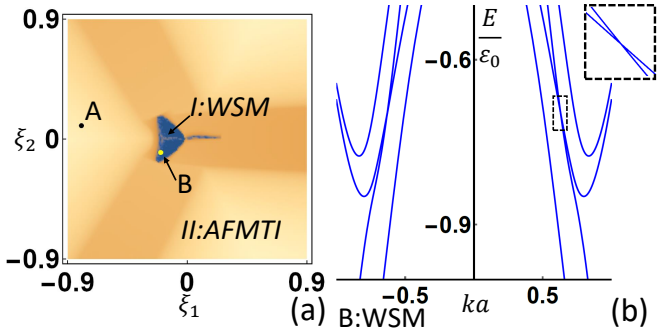

FIG. 8. (a) shows the approximate direct gap distribution of the system on $\xi_1 - \xi_2$ parameter plane with non-zero $\xi_{3,4,5}$. The color is scaled by the logarithm with base 10 of the direct gap of system. Lighter color indicates larger gap, and gaps smaller than 10^{-5} are marked with the same color as that of 10^{-5}. The graph shows two regions: (i) region I which should be WSM phase, and (ii) region II which should be AFMTI phase. (b) shows the bulk dispersion along the line connecting two Weyl points at $\mathbf{k}a = \pm(-0.23, -0.21, 0.55)$. The Weyl points belong to point B in Fig.8a with $(\xi_1, \xi_2) = (-0.2, -0.1)\varepsilon_0$. The inset is a zoom-in version for $\mathbf{k}a = (-0.23, -0.21, 0.55)$.

H_{Kane} in this section. With the anti-ferromagnetic ordering, the full Hamitonian takes the form

$$H_{Kane}^{AFM} = \left(\begin{array}{c|c} H_{\Gamma_6}(\mathbf{k}) & V \\ \hline V^\dagger & H_{\Gamma_8}(\mathbf{k}) + H_{AFM} \end{array}\right), \qquad (9)$$

which can be diagonalized numerically to extract the energy dispersion.

To systematically understand the AFM term in the Kane model, we consider different ξ_i terms $(i = 1, \ldots, 5)$ in Eq.7, separately. We notice that applying three-fold rotational symmetry $C_3(111)$ to H_{AFM} is equivalent to performing the following transformations: $(\xi_1, \xi_2) \to (-\frac{1}{2}\xi_1 - \frac{\sqrt{3}}{2}\xi_2, \frac{\sqrt{3}}{2}\xi_1 - \frac{1}{2}\xi_2)$ and $(\xi_3, \xi_4, \xi_5) \to (\xi_4, \xi_5, \xi_3)$, which means $\xi_{1,2}$ are related with each other by $C_3(111)$ and so do $\xi_{3,4,5}$. Therefore, we study the direct band gap as a function of (i) ξ_1 and ξ_2 for $\xi_{3,4,5} = 0$ in which case the effective Hamiltonian H_{Kane}^{AFM} in Eq.9 preserves two-fold rotation symmetry along the x,y,z axes, or (ii) ξ_1 and ξ_3 for $\xi_{2,4,5} = 0$ in which case the effective model H_{Kane}^{AFM} preserves $\pi_{1\bar{1}0}$, two-fold rotation along z axis and mirror symmetry perpendicular to (110). The phase diagrams for the case (i) and (ii) are shown in Fig.7a and Fig.7b, respectively, from which one can find both the gapless phases existing in the blue region (the region I) and the gapped phases in the three yellow regions (the region II). Detailed parameters for our calculation can be found in Tab.X and Tab.XI in Appendix F. We notice that ξ_1 term takes the same form as the strain term described in Ref.[47]. Therefore, on the line $\xi_2 = 0$ in Fig.7a or the line $\xi_3 = 0$ in Fig.7b, we expect the gapless and gapped phases should be equivalent to the corresponding ones studied for strained HgTe and half-Heusler materials[47]. To verify the nature of gapless and insulating phases, we calculate the energy dispersion for two typical sets of parameters: the point A with $(\xi_1, \xi_3) = (-0.8, 0.1)\varepsilon_0$ and B with $(\xi_1, \xi_3) = (-0.1, 0.3)\varepsilon_0$ in Fig.7b. A non-zero bulk direct gap is found for the point A and thus we consider an approximately semi-infinite configuration and plot the local density of states on (001) surface, as shown in Fig.7c. A helical surface mode is found in the bulk gap and is protected by the S symmetry instead of the time reversal symmetry due to the anti-ferromagnetic ordering, thus giving rise to a realization of AFMTI phase. The gapless phase at point B is found to be WSM phase and the bulk dispersion is shown Fig.7d with the Weyl points located at the momenta $\mathbf{k}a = \pm(0.89, 0.35, 0)$ (or equivalent $\mathbf{k}a = \pm(-0.35, -0.89, 0)$).

Below we emphasize that the AFMTI phase is quite robust in this system. The phase diagram for $\xi_1 - \xi_2$ is shown in Fig.8a for $(\xi_3, \xi_4, \xi_5) = (-0.01, 0.023, 0.026)\varepsilon_0$. Other parameters are listed in Tab.XII in Appendix F. We notice that after introducing non-zero $\xi_{3,4,5}$ which breaks all C_{3v} symmetries and their combinations with half translation, the previous gapless phase region I in Fig.7a shrinks to a smaller region I in Fig.8a, while the region II of AFMTI phase is greatly extended. In

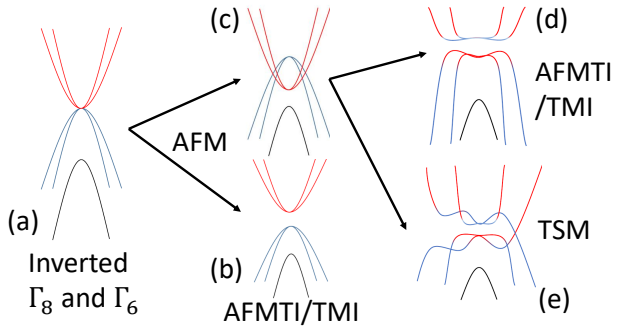

FIG. 9. Schematic physical picture of evolution of electronic band structures of half-Heusler compounds with AFM. (a) is for the band ordering without AFM, while (b) and (c) are normal and inverted band ordering between different Γ_8 bands after including AFM. Depending on detailed parameters for AFM, the inverted band structures due to AFM can either be gapped or be gapless, leading to (d) topological insulating phases or (e) TSM phases.

the region I, Weyl points are found (not exclusively) at $\mathbf{k}a = \pm(-0.23, -0.21, 0.55)$ for point B of Fig.8a, as shown in Fig.8b. The local density of states calculation on (001) surface for point A in Fig.8a with $(\xi_1, \xi_2) = (-0.8, 0.1)\varepsilon_0$ gives very similar graph as Fig.7c, thus demonstrating the AFMTI phase in the region II. Given the large region in the parameter space for the realization of AFMTI phases, we can conclude that anti-ferromagnetic half-Heusler materials provide a robust material realization of the AFMTI phase. Moreover, if mirror or non-symmorphic symmetry exists, anti-ferromagnetic half-Heusler materials can also provide a robust material realization of anti-ferromagnetic mirror or non-symmorphic topological insulator phase, which has not been demonstrated in experiments.

V. Conclusion

Based on the above studies of the four-band and six-band Kane models, we can summarize the overall physical picture for electronic structures of anti-ferromagnetic half-Heusler compounds in Fig.9. Without AFM, the band ordering of Γ_6 and Γ_8 bands are inverted and the Fermi energy lies at the four fold degenerate point ($\mathbf{k} = 0$) of Γ_8 bands, leading to a critical semimetal phase shown in Fig.9a. With AFM, four-fold degeneracy of Γ_8 bands at Γ point is removed. The band structure of four Γ_8 bands can be either normal (Fig.9b) or inverted (Fig.9c), depending on the detailed form and parameters of AFM terms. When the band ordering of Γ_8 bands is normal, it is trivial for the four-band model but non-trivial for the six-band Kane model due to the inversion between the Γ_6 and Γ_8 bands, leading to either AFMTI phase or TMI phase. When the Γ_8 band ordering is inverted, the AFM terms can either lead to a full inverted band gap (AFMTI or TMI phase in Fig.9d) or preserve certain gapless points in the momentum space (the TSM phase in Fig.9e). In either situation, we find that anti-ferromagnetic half-Heusler compounds are topologically non-trivial. Thus, our work demonstrates that half-Heusler materials with AFM provide a platform for a robust realization of anti-ferromagnetic topological phases, either WSM phase or AFMTI phase, in a wide parameter regime.

The AFMTI phase was first proposed in Ref.[31] based on a four band toy model and our results have shown this interesting topological phase indeed can exist in anti-ferromagnetic half-Heusler materials. We notice that the first principles calculation in combining with tight-binding model has been adopted for the AFM GdPtBi[60], in which a semi-metal phase is found. However, the topological nature of this semi-metal phase has not been extracted and our results identify the existence of Weyl points in this semimetal phase. In addition, the authors use the representation of crystal symmetry group to label each band, aiming in identifying band inversion. We believe this approach is insufficient for the AFMTI phase since this topological phase is protected by the S symmetry which is not included in the crystal symmetry group. Thus, the AFMTI phase cannot be identified from the crystal symmetry representation. Our results suggest that the AFMTI phase can exist in the G-type anti-ferromagnetic system, which is identified to be topologically trivial in Ref.[60]. In the existing experiments, Weyl semi-metal phase has been unveiled in GdPtBi under an external magentic field through the observation of a large anomalous Hall angle[49,50], large negative magnetoresistance[48,49] and the strong suppression of thermopower[48]. Our results suggest Weyl semimetal phase may already occur even in absence of external magnetic fields. In addition, nodal line fermions, type-B triply degenerate fermions and topological mirror or glide insulators, are also possible in certain parameter regimes when magnetic moments of anti-ferromagnetic ordering are along some specific directions. The topological surface states or surface Fermi arcs in these topological phases can be extracted from angle-resolved photoemission spectroscopy or quasi-particle spectrum from the scanning tunneling microscopy[1,2,12]. Our generalized Kane model also provides a basis for the future study of magnetic, transport or optical phenomena in this class of materials. Furthermore, we notice that superconductivity can coexist with anti-ferromagnetism in RPdBi(R=Tb,Ho,Dy,Er)[51,55,56]. Thus, it is interesting to ask if topological superconductivity can be realized in these materials.

VI. Acknowledgment

We would like to thank Claudia Felser, Hao Yang, Rui-Xing Zhang, Jian-Xiao Zhang, Qing-Ze Wang, Yang Ge and Di Xiao for helpful discussion. C.-X.L. acknowledges the support from Office of Naval Research (Grant No.

N00014-15-1-2675). B.Y. acknowledges support of the Ruth and Herman Albert Scholars Program for New Scientists in Weizmann Institute of Science, Israel.

* E-Mail: cxl56@psu.edu

[1] X.-L. Qi and S.-C. Zhang, Rev. Mod. Phys. **83**, 1057 (2011).
[2] M. Z. Hasan and C. L. Kane, Rev. Mod. Phys. **82**, 3045 (2010).
[3] L. Fu, Phys. Rev. Lett. **106**, 106802 (2011).
[4] H. Lin, L. A. Wray, Y. Xia, S. Xu, S. Jia, R. J. Cava, A. Bansil, and M. Z. Hasan, Nat Mater **9**, 546 (2010).
[5] Y. Tanaka, Z. Ren, T. Sato, K. Nakayama, S. Souma, T. Takahashi, K. Segawa, and Y. Ando, Nat Phys **8**, 800 (2012).
[6] S.-Y. Xu, C. Liu, N. Alidoust, M. Neupane, D. Qian, I. Belopolski, J. Denlinger, Y. Wang, H. Lin, L. Wray, *et al.*, Nature communications **3**, 1192 (2012).
[7] T. H. Hsieh, H. Lin, J. Liu, W. Duan, A. Bansil, and L. Fu, Nature communications **3**, 982 (2012).
[8] J. Alicea, Reports on Progress in Physics **75**, 076501 (2012).
[9] A. P. Schnyder, S. Ryu, A. Furusaki, and A. W. Ludwig, Physical Review B **78**, 195125 (2008).
[10] R. M. Lutchyn, J. D. Sau, and S. D. Sarma, Physical review letters **105**, 077001 (2010).
[11] C. Beenakker, Annual Review of Condensed Matter Physics **4**, 113 (2013).
[12] B. Yan and C. Felser, Annual Review of Condensed Matter Physics (2016).
[13] L. Yang, Z. Liu, Y. Sun, H. Peng, H. Yang, T. Zhang, B. Zhou, Y. Zhang, Y. Guo, M. Rahn, *et al.*, Nature physics **11**, 728 (2015).
[14] X. Wan, A. M. Turner, A. Vishwanath, and S. Y. Savrasov, Phys. Rev. B **83**, 205101 (2011).
[15] H. Weng, C. Fang, Z. Fang, B. A. Bernevig, and X. Dai, Phys. Rev. X **5**, 011029 (2015).
[16] S.-M. Huang, S.-Y. Xu, I. Belopolski, C.-C. Lee, G. Chang, B. Wang, N. Alidoust, G. Bian, M. Neupane, C. Zhang, *et al.*, Nature communications **6** (2015).
[17] S.-Y. Xu, I. Belopolski, N. Alidoust, M. Neupane, G. Bian, C. Zhang, R. Sankar, G. Chang, Z. Yuan, C.-C. Lee, *et al.*, Science **349**, 613 (2015).
[18] B. Lv, H. Weng, B. Fu, X. Wang, H. Miao, J. Ma, P. Richard, X. Huang, L. Zhao, G. Chen, *et al.*, Physical Review X **5**, 031013 (2015).
[19] Y. Xu, F. Zhang, and C. Zhang, Phys. Rev. Lett. **115**, 265304 (2015).
[20] A. A. Soluyanov, D. Gresch, Z. Wang, Q. Wu, M. Troyer, X. Dai, and B. A. Bernevig, Nature **527**, 495 (2015).
[21] Z. Wang, Y. Sun, X.-Q. Chen, C. Franchini, G. Xu, H. Weng, X. Dai, and Z. Fang, Phys. Rev. B **85**, 195320 (2012).
[22] Z. Liu, B. Zhou, Y. Zhang, Z. Wang, H. Weng, D. Prabhakaran, S.-K. Mo, Z. Shen, Z. Fang, X. Dai, *et al.*, Science **343**, 864 (2014).
[23] Z. Wang, H. Weng, Q. Wu, X. Dai, and Z. Fang, Phys. Rev. B **88**, 125427 (2013).
[24] A. A. Burkov, M. D. Hook, and L. Balents, Phys. Rev. B **84**, 235126 (2011).
[25] B. Bradlyn, J. Cano, Z. Wang, M. Vergniory, C. Felser, R. Cava, and B. A. Bernevig, Science **353**, aaf5037 (2016).
[26] B. Yan and S.-C. Zhang, Reports on Progress in Physics **75**, 096501 (2012).
[27] F. D. M. Haldane, Physical Review Letters **61**, 2015 (1988).
[28] C.-X. Liu, X.-L. Qi, X. Dai, Z. Fang, and S.-C. Zhang, Physical review letters **101**, 146802 (2008).
[29] C.-Z. Chang, J. Zhang, X. Feng, J. Shen, Z. Zhang, M. Guo, K. Li, Y. Ou, P. Wei, L.-L. Wang, *et al.*, Science **340**, 167 (2013).
[30] R. Yu, W. Zhang, H.-J. Zhang, S.-C. Zhang, X. Dai, and Z. Fang, Science **329**, 61 (2010).
[31] R. S. K. Mong, A. M. Essin, and J. E. Moore, Phys. Rev. B **81**, 245209 (2010).
[32] C. Fang, M. J. Gilbert, and B. A. Bernevig, Physical Review B **88**, 085406 (2013).
[33] T. Yoshida, R. Peters, S. Fujimoto, and N. Kawakami, Physical Review B **87**, 085134 (2013).
[34] L.-H. Wu, Q.-F. Liang, and X. Hu, Journal of the Physical Society of Japan **85**, 014706 (2015).
[35] F. Bègue, P. Pujol, and R. Ramazashvili, arXiv preprint arXiv:1604.01707 (2016).
[36] W. Brzezicki and M. Cuoco, arXiv preprint arXiv:1609.06916 (2016).
[37] S. M. Young and B. J. Wieder, arXiv preprint arXiv:1609.06738 (2016).
[38] T. Graf, S. S. Parkin, and C. Felser, IEEE Transactions on Magnetics **47**, 367 (2011).
[39] H. Lin, L. A. Wray, Y. Xia, S. Xu, S. Jia, R. J. Cava, A. Bansil, and M. Z. Hasan, Nature materials **9**, 546 (2010).
[40] S. Chadov, X. Qi, J. Kübler, G. H. Fecher, C. Felser, and S. C. Zhang, Nature materials **9**, 541 (2010).
[41] D. Xiao, Y. Yao, W. Feng, J. Wen, W. Zhu, X.-Q. Chen, G. M. Stocks, and Z. Zhang, Phys. Rev. Lett. **105**, 096404 (2010).
[42] W. Al-Sawai, H. Lin, R. S. Markiewicz, L. A. Wray, Y. Xia, S.-Y. Xu, M. Z. Hasan, and A. Bansil, Phys. Rev. B **82**, 125208 (2010).
[43] B. Yan and A. de Visser, MRS Bulletin **39**, 859 (2014).
[44] Z. K. Liu, L. X. Yang, S.-C. Wu, C. Shekhar, J. Jiang, H. F. Yang, Y. Zhang, S.-K. Mo, Z. Hussain, B. Yan, C. Felser, and Y. L. Chen, Nature Communications **7**, 12924 (2016), article.
[45] J. Logan, S. Patel, S. Harrington, C. Polley, B. Schultz, T. Balasubramanian, A. Janotti, A. Mikkelsen, and C. Palmstrøm, Nature communications **7** (2016).
[46] J. Cano, B. Bradlyn, Z. Wang, M. Hirschberger, N. Ong, and B. Bernevig, arXiv preprint arXiv:1604.08601 (2016).
[47] J. Ruan, S.-K. Jian, H. Yao, H. Zhang, S.-C. Zhang, and D. Xing, Nature communications **7** (2016).
[48] M. Hirschberger, S. Kushwaha, Z. Wang, Q. Gibson, S. Liang, C. A. Belvin, B. A. Bernevig, R. J. Cava, and N. P. Ong, Nat Mater **15**, 1161 (2016), letter.
[49] C. Shekhar, A. K. Nayak, S. Singh, N. Kumar, S.-C. Wu, Y. Zhang, A. C. Komarek, E. Kampert, Y. Sk-

ourski, J. Wosnitza, *et al.*, arXiv preprint arXiv:1604.01641 (2016).
[50] T. Suzuki, R. Chisnell, A. Devarakonda, Y.-T. Liu, W. Feng, D. Xiao, J. Lynn, and J. Checkelsky, Nature Physics (2016).
[51] Y. Pan, A. Nikitin, T. Bay, Y. Huang, C. Paulsen, B. Yan, and A. de Visser, EPL (Europhysics Letters) **104**, 27001 (2013).
[52] K. Gofryk, D. Kaczorowski, T. Plackowski, A. Leithe-Jasper, and Y. Grin, Phys. Rev. B **84**, 035208 (2011).
[53] R. A. Müller, N. R. Lee-Hone, L. Lapointe, D. H. Ryan, T. Pereg-Barnea, A. D. Bianchi, Y. Mozharivskyj, and R. Flacau, Phys. Rev. B **90**, 041109 (2014).
[54] A. M. Nikitin, Y. Pan, X. Mao, R. Jehee, G. K. Araizi, Y. K. Huang, C. Paulsen, S. C. Wu, B. H. Yan, and A. de Visser, Journal of Physics: Condensed Matter **27**, 275701 (2015).
[55] Y. Nakajima, R. Hu, K. Kirshenbaum, A. Hughes, P. Syers, X. Wang, K. Wang, R. Wang, S. R. Saha, D. Pratt, *et al.*, Science advances **1**, e1500242 (2015).
[56] O. Pavlosiuk, D. Kaczorowski, X. Fabreges, A. Gukasov, and P. Wiśniewski, Scientific reports **6** (2016).
[57] O. Pavlosiuk, D. Kaczorowski, and P. Wiśniewski, Acta Physica Polonica A **130**, 573 (2016).
[58] Z. Zhu, G. W. Winkler, Q. Wu, J. Li, and A. A. Soluyanov, Phys. Rev. X **6**, 031003 (2016).
[59] P. C. Canfield, J. Thompson, W. Beyermann, A. Lacerda, M. Hundley, E. Peterson, Z. Fisk, and H. Ott, Journal of applied physics **70**, 5800 (1991).
[60] Z. Li, H. Su, X. Yang, and J. Zhang, Physical Review B **91**, 235128 (2015).
[61] R. Winkler, S. Papadakis, E. De Poortere, and M. Shayegan, *Spin-Orbit Coupling in Two-Dimensional Electron and Hole Systems*, Vol. 41 (Springer, 2003).
[62] S. Murakami, New Journal of Physics **9**, 356 (2007).
[63] M. L. Sancho, J. L. Sancho, J. L. Sancho, and J. Rubio, Journal of Physics F: Metal Physics **15**, 851 (1985).
[64] J. C. Y. Teo, L. Fu, and C. L. Kane, Phys. Rev. B **78**, 045426 (2008).
[65] G. E. Volovik, *The universe in a helium droplet*, Vol. 117 (Oxford University Press on Demand, 2003).
[66] G. Volovik, in *Quantum analogues: from phase transitions to black holes and cosmology* (Springer, 2007) pp. 31–73.
[67] G. E. Volovik, in *Analogue Gravity Phenomenology* (Springer, 2013) pp. 343–383.
[68] Y.-H. Chan, C.-K. Chiu, M. Chou, and A. P. Schnyder, Physical Review B **93**, 205132 (2016).
[69] G. Burns, *Introduction to group theory with applications: materials science and technology* (Academic Press, 2014).
[70] B. A. Bernevig, T. L. Hughes, and S.-C. Zhang, Science **314**, 1757 (2006).
[71] J. C. Slater and G. F. Koster, Phys. Rev. **94**, 1498 (1954).
[72] A. Gelessus, W. Thiel, and W. Weber, J. chem. Educ **72**, 505 (1995).
[73] M. I. Aroyo, J. M. Perez-Mato, C. Capillas, E. Kroumova, S. Ivantchev, G. Madariaga, A. Kirov, and H. Wondratschek, Zeitschrift für Kristallographie-Crystalline Materials **221**, 15 (2006).

A. Tight-Binding Model and its relationship to the Kane model

In this section, we will describe a tight-binding model for our anti-ferromagnetic half-Heusler materials, from which we can justify the extend Kane model that we derived by symmetry principles and used for the low energy physics in Sec.II in the main text. For simplicity, we take the anti-ferromagnetic half-Heusler material ErPdBi as an example and assume it has anti-ferromagnetic structure of GdPtBi. We consider nine orbitals $|Bi, s\rangle$, $|Pd, s\rangle$, $|Pd, p_x\rangle$, $|Pd, p_y\rangle$, $|Pd, p_z\rangle$, $|Er, s\rangle$, $|Er, d_{xy}\rangle$, $|Er, d_{yz}\rangle$ and $|Er, d_{zx}\rangle$ to construct the tight-binding model for this material. Due to the doubling of the unit cell along $\mathbf{a}_3'$, all the orbitals are labeled as $|n, i\rangle$, where n stands for atoms and orbitals and $i = 1, 2$ labels two sub-lattices that are related by $T_{\mathbf{a}_3'}$. We only considered the hopping terms between the nearest neighbor atoms, including Bi, Pd and Er atoms[71], giving rise to a 18 by 18 Hamiltonian $H_{hopping}$. In order to include AFM term and spin-orbit term, we need to consider spin degree of freedom and the hopping term is block diagonal with each block given by $H_{hopping}$ in the spin space. The AFM term is given by $H_{AFM} = (-1)^i \mathbf{M} \cdot \mathbf{S}$ with $i = 1, 2$ for two sets of cells. Here $\mathbf{M}$ is the mean field value for anti-ferromagnetic magnetic moments and $\mathbf{S}$ labels electron spin. The spin-orbit coupling term takes the form $H_{so} = \mathbf{S} \cdot \mathbf{L}$, where $\mathbf{L}$ denotes the angular momentum operator that acts on the oribtal (s, p, d orbitals).

	E	$8C_3$	$3C_2$	$6S_4$	$6\sigma_d$	linear, rotations	quadratic
A_1	1	1	1	1	1		$x^2+y^2+z^2$
A_2	1	1	1	-1	-1		
E	2	-1	2	0	0		$(2z^2-x^2-y^2, x^2-y^2)$
T_1	3	0	-1	1	-1	(R_x, R_y, R_z)	
T_2	3	0	-1	-1	1	(x, y, z)	(xy, xz, yz)

FIG. 10. Character Table of T_d group[72,73]. p_x, p_y, p_z orbitals and d_{xy}, d_{yz}, d_{zx} orbitals belong to T_2 representation.

The above 36 by 36 tight-binding Hamiltonian is complicated and we are not interested in using this model for realistic calculation here. Instead, we hope to use this model to justify the form of the extended Kane model that we derived from the symmetry principle in the main text. We need to transform the basis wave functions into the ones used for the Kane model, which can be achieved by the following steps. (1) The basis wave functions of the Kane model only include two s orbital type of bands and 6 p orbital type of bands after taking into account spin degree of freedom. There-

fore, we need to first reduce the number of basis wave functions. Since both the p_x, p_y, p_z and d_{xy}, d_{yz}, d_{zx} orbitals belong to T_2 representation of the T_d group (The representation table of T_d group is shown in Fig.10), the basis wave functions should be a linear combination of the p and d orbitals, which are given by $|\gamma, i, \sigma\rangle = P_1 |Pd, p_\alpha, i, \sigma\rangle + P_2 |Er, d_\beta, i, \sigma\rangle$, where $i = 1, 2$, $\sigma = \uparrow, \downarrow$ and $(\gamma, \alpha, \beta) = (X, x, yz), (Y, y, zx), (Z, z, xy)$. For the s orbital type of bands, the basis wave functions take the form $|S, i, \sigma\rangle = S_1 |Bi, s, i, \sigma\rangle + S_2 |Pd, s, i, \sigma\rangle + S_3 |Er, s, i, \sigma\rangle$, where $i = 1, 2$ and $\sigma = \uparrow, \downarrow$. Here we still keep the sub-lattice index $i = 1, 2$ and the number of basis wave functions are reduced to 16. (2) The basis wave functions of the Kane model is chosen to be the eigenstates of total angular momentum operator because of strong spin-orbit coupling. Therefore, we apply a similar transformation to our basis wave functions here, as listed below:

$$
\begin{array}{c}
\left|\Gamma_6, \frac{1}{2}, 1\right\rangle = i\,|S, \uparrow, 1\rangle \\
\left|\Gamma_6, -\frac{1}{2}, 1\right\rangle = i\,|S, \downarrow, 1\rangle \\
\left|\Gamma_8, \frac{3}{2}, 1\right\rangle = -\frac{1}{\sqrt{2}}\,|X, \uparrow, 1\rangle + \frac{i}{\sqrt{2}}\,|Y, \uparrow, 1\rangle \\
\left|\Gamma_8, \frac{1}{2}, 1\right\rangle = -\frac{1}{\sqrt{6}}\,|X, \downarrow, 1\rangle + \frac{i}{\sqrt{6}}\,|Y, \downarrow, 1\rangle + \sqrt{\frac{2}{3}}\,|Z, \uparrow, 1\rangle \\
\left|\Gamma_8, -\frac{1}{2}, 1\right\rangle = \frac{1}{\sqrt{6}}\,|X, \uparrow, 1\rangle + \frac{i}{\sqrt{6}}\,|Y, \uparrow, 1\rangle + \sqrt{\frac{2}{3}}\,|Z, \downarrow, 1\rangle \\
\left|\Gamma_8, -\frac{3}{2}, 1\right\rangle = \frac{1}{\sqrt{2}}\,|X, \downarrow, 1\rangle + \frac{i}{\sqrt{2}}\,|Y, \downarrow, 1\rangle \\
\left|\Gamma_7, \frac{1}{2}, 1\right\rangle = -\frac{1}{\sqrt{3}}\,|X, \downarrow, 1\rangle + \frac{i}{\sqrt{3}}\,|Y, \downarrow, 1\rangle - \frac{1}{\sqrt{3}}\,|Z, \uparrow, 1\rangle \\
\left|\Gamma_7, -\frac{1}{2}, 1\right\rangle = -\frac{1}{\sqrt{3}}\,|X, \uparrow, 1\rangle - \frac{i}{\sqrt{3}}\,|Y, \uparrow, 1\rangle + \frac{1}{\sqrt{3}}\,|Z, \downarrow, 1\rangle \\
\left|\Gamma_6, \frac{1}{2}, 2\right\rangle = i\,|S, \uparrow, 2\rangle \\
\left|\Gamma_6, -\frac{1}{2}, 2\right\rangle = i\,|S, \downarrow, 2\rangle \\
\left|\Gamma_8, \frac{3}{2}, 2\right\rangle = -\frac{1}{\sqrt{2}}\,|X, \uparrow, 2\rangle + \frac{i}{\sqrt{2}}\,|Y, \uparrow, 2\rangle \\
\left|\Gamma_8, \frac{1}{2}, 2\right\rangle = -\frac{1}{\sqrt{6}}\,|X, \downarrow, 2\rangle + \frac{i}{\sqrt{6}}\,|Y, \downarrow, 2\rangle + \sqrt{\frac{2}{3}}\,|Z, \uparrow, 2\rangle \\
\left|\Gamma_8, -\frac{1}{2}, 2\right\rangle = \frac{1}{\sqrt{6}}\,|X, \uparrow, 2\rangle + \frac{i}{\sqrt{6}}\,|Y, \uparrow, 2\rangle + \sqrt{\frac{2}{3}}\,|Z, \downarrow, 2\rangle \\
\left|\Gamma_8, -\frac{3}{2}, 2\right\rangle = \frac{1}{\sqrt{2}}\,|X, \downarrow, 2\rangle + \frac{i}{\sqrt{2}}\,|Y, \downarrow, 2\rangle \\
\left|\Gamma_7, \frac{1}{2}, 2\right\rangle = -\frac{1}{\sqrt{3}}\,|X, \downarrow, 2\rangle + \frac{i}{\sqrt{3}}\,|Y, \downarrow, 2\rangle - \frac{1}{\sqrt{3}}\,|Z, \uparrow, 2\rangle \\
\left|\Gamma_7, -\frac{1}{2}, 2\right\rangle = -\frac{1}{\sqrt{3}}\,|X, \uparrow, 2\rangle - \frac{i}{\sqrt{3}}\,|Y, \uparrow, 2\rangle + \frac{1}{\sqrt{3}}\,|Z, \downarrow, 2\rangle
\end{array}
,
$$

where $1, 2$ are sub-lattice indexes. (3) Since the low energy physics only occurs at the Γ point ($\mathbf{k} = 0$) for the Kane model, we only need to consider the bonding states between two sub-lattices. The 8 bonding basis wave functions are given by $|\Lambda, \sigma\rangle = \frac{1}{\sqrt{2}}(|\Lambda, \sigma, 1\rangle + |\Lambda, \sigma, 2\rangle)$, where $\Lambda = \Gamma_{6,7,8}$ and $\sigma = \pm\frac{1}{2}$,or including $\pm\frac{3}{2}$ for Γ_8. By projecting the full tight-binding Hamiltonian into the six basis wave functions, including $|\Gamma_6, \frac{1}{2}\rangle$, $|\Gamma_6, -\frac{1}{2}\rangle$, $|\Gamma_8, \frac{3}{2}\rangle$, $|\Gamma_8, \frac{1}{2}\rangle$, $|\Gamma_8, -\frac{1}{2}\rangle$ and $|\Gamma_8, -\frac{3}{2}\rangle$ and expand the resulting Hamiltonian to the second order in both $\mathbf{k}$ and $\mathbf{M}$, we reproduce the extended Kane model Hamiltonian with the anti-ferromagnetic ordering derived by the symmetry principles in our main text.

B. Irreducible Representations of C_{3v} group

In this section, we will use the representation table of the C_{3v} group to classify the polynomials of $\mathbf{k}$ and $\mathbf{M}$,

	E	$2C_3$	$3\sigma_v$
A_1	$+1$	$+1$	$+1$
A_2	$+1$	$+1$	-1
E	$+2$	-1	0

TABLE II. Character table of C_{3v} group.[72,73]

as well as all the four by four matrices for the Γ_8 basis wave functions, which is used to construct the effective low energy Hamiltonian for our system in Sec.II.

The C_{3v} group can be generated by two operations, three-fold rotation and mirror operation. For the lattice considered here, the three-fold rotation is along the (111) axis, denoted as $C_3(111)$, and mirror operation is with repsect to the $(1, -1, 0)$ plane, denoted as $\pi_{1\bar{1}0}$, where $\bar{1}$ means -1. It has three irreducible representations A_1, A_2 and E and its character table is shown in Tab.II.

Since magnetic moments of the anti-ferromagnetic ordering come from the d orbitals of Er atoms, we only focus on the the Γ_8 bands which contains d orbitals of Er atoms. We need to construct the generator operations of the C_{3v} group on the Γ_8 bands. To achieve that, we notice the angular momentum operators $J_{x,y,z}$ for spin-$\frac{3}{2}$ states can be represented by the four by four matrices

$$
J_x \doteq \begin{pmatrix} 0 & \frac{\sqrt{3}}{2} & 0 & 0 \\ \frac{\sqrt{3}}{2} & 0 & 1 & 0 \\ 0 & 1 & 0 & \frac{\sqrt{3}}{2} \\ 0 & 0 & \frac{\sqrt{3}}{2} & 0 \end{pmatrix}
$$

$$
J_y \doteq \begin{pmatrix} 0 & -\frac{i\sqrt{3}}{2} & 0 & 0 \\ \frac{i\sqrt{3}}{2} & 0 & -i & 0 \\ 0 & i & 0 & -\frac{i\sqrt{3}}{2} \\ 0 & 0 & \frac{i\sqrt{3}}{2} & 0 \end{pmatrix}
$$

$$
J_z \doteq \begin{pmatrix} \frac{3}{2} & 0 & 0 & 0 \\ 0 & \frac{1}{2} & 0 & 0 \\ 0 & 0 & -\frac{1}{2} & 0 \\ 0 & 0 & 0 & -\frac{3}{2} \end{pmatrix}.
$$

As a result, the $C_3(111)$ and $\pi_{1\bar{1}0}$ operations are given by

$$
C_3(111) \doteq \exp(-i\frac{J_x + J_y + J_z}{\sqrt{3}}\frac{2\pi}{3})
$$

$$
\pi_{1\bar{1}0} \doteq -\exp(-i\frac{J_x - J_y}{\sqrt{2}}\pi).
$$

In addition, time reversal operator and half translation operator $T_{\mathbf{a}'_3}$ are interesting to us since the anti-ferromagnetic ordering preserves the S symmetry which is the combination of these two operators. On the four basis

C_{3v}	Combinations of J_i's	Θ	$T_{\mathbf{a}_3'}$
A_1	$J_x^2+J_y^2+J_z^2$	$+$	$+$
A_1	$J_{xy}+J_{yz}+J_{zx}$	$+$	$+$
A_1	$V_x+V_y+V_z$	$-$	$+$
A_2	J_{xyz}	$-$	$+$
A_2	$J_x+J_y+J_z$	$-$	$+$
A_2	$J_x^3+J_y^3+J_z^3$	$-$	$+$
E	$\sqrt{3}(-J_x+J_y);\ 2J_z-J_x-J_y$	$-$	$+$
E	$\sqrt{3}(-J_x^3+J_y^3);\ 2J_z^3-J_x^3-J_y^3$	$-$	$+$
E	$2V_z-V_x-V_y;\ \sqrt{3}(V_x-V_y)$	$-$	$+$
E	$2J_z^2-J_x^2-J_y^2;\ \sqrt{3}(J_x^2-J_y^2)$	$+$	$+$
E	$2J_{xy}-J_{yz}-J_{zx};\ \sqrt{3}(J_{yz}-J_{zx})$	$+$	$+$

TABLE III. This table shows combinations of J_i's, their corresponding C_{3v} irreducible representations and their parities under time reversal Θ and half translation $T_{\mathbf{a}_3'}$. The first column shows the corresponding irreducible representations of C_3v. The second column shows the expressions of combinations. The third and fourth columns show how signs of those combinations change under Θ and $T_{\mathbf{a}_3'}$, where "+" means no sign change and "−" means the sign should change.

C_{3v}	Combinations of k_i's or M_i's	Θ	$T_{\mathbf{a}_3'}$
A_1	$k_x+k_y+k_z$	$-$	$+$
A_1	$k_x^2+k_y^2+k_z^2$	$+$	$+$
A_1	$k_xk_y+k_yk_z+k_zk_x$	$+$	$+$
A_1	$M_x^2+M_y^2+M_z^2$	$+$	$+$
A_1	$M_xM_y+M_yM_z+M_zM_x$	$+$	$+$
A_2	$M_x+M_y+M_z$	$-$	$-$
E	$2k_z-k_x-k_y;\ \sqrt{3}(k_x-k_y)$	$-$	$+$
E	$2k_z^2-k_x^2-k_y^2;\ \sqrt{3}(k_x^2-k_y^2)$	$+$	$+$
E	$2k_xk_y-k_yk_z-k_zk_x;\ \sqrt{3}(k_yk_z-k_zk_x)$	$+$	$+$
E	$\sqrt{3}(-M_x+M_y);\ 2M_z-M_x-M_y$	$-$	$-$
E	$2M_z^2-M_x^2-M_y^2;\ \sqrt{3}(M_x^2-M_y^2)$	$+$	$+$
E	$2M_xM_y-(M_y+M_x)M_z;\ \sqrt{3}M_z(M_y-M_x)$	$+$	$+$

TABLE IV. This table shows combinations of k_i's or M_i's, their corresponding C_{3v} irreducible representations and their parities under time reversal Θ and half translation $T_{\mathbf{a}_3'}$. The first column shows the corresponding irreducible representations of C_{3v}. The second column shows the expressions of combinations. The third and fourth columns show how signs of those combinations change under Θ and $T_{\mathbf{a}_3'}$, where "+" means no sign change and "−" means the sign should change.

of the Γ_8 bands, we find time reversal operator writeen as

$$\Theta \doteq \begin{pmatrix} 0 & 0 & 0 & -1 \\ 0 & 0 & 1 & 0 \\ 0 & -1 & 0 & 0 \\ 1 & 0 & 0 & 0 \end{pmatrix} \hat{K},$$

with the complex conjuate $\hat{K}$ and the half translation $T_{\mathbf{a}_3'}$ taking the form of an identity matrix

$$T_{\mathbf{a}_3'} \doteq \begin{pmatrix} 1 & 0 & 0 & 0 \\ 0 & 1 & 0 & 0 \\ 0 & 0 & 1 & 0 \\ 0 & 0 & 0 & 1 \end{pmatrix},$$

because of the bonding state nature of two sub-lattices for the four Γ_8 bands. As a consequence, the S symmetry takes the same form as the time reversal symmetry on the four Γ_8 basis.

16 four-by-four matrices can be constructed by three spin $\frac{3}{2}$ matrices $J_{x,y,z}$ as J_x, J_y, J_z, J_x^2, J_y^2, J_z^2, $J_{xy}=\{J_x,J_y\}/2$, $J_{yz}=\{J_y,J_z\}/2$, $J_{zx}=\{J_z,J_x\}/2$, J_x^3, J_y^3, J_z^3, $V_x=\{J_y^2-J_z^2,J_x\}/2$, $V_y=\{J_z^2-J_x^2,J_y\}/2$, $V_z=\{J_x^2-J_y^2,J_z\}/2$ and $J_{xyz}=J_xJ_yJ_z+J_zJ_yJ_x$. The linear combinations of these 16 matrices belong to different irreducible representations of the C_{3v} group and we list the corresponding representations in in Tab.III.

Next we will classify all the polynomials of $\mathbf{k}$ and $\mathbf{M}$ according to the irreducible representations of the C_{3v} group[61]. The representations for the polynomials of the momentum $\mathbf{k}$ and anti-ferromagnetic magnetic moments $\mathbf{M}$ are listed in Tab.IV.

C. Gapless Conditions for the Hamiltonian $H_0 + H_{AFM}$

In this section, we will present the detailed analysis of the conditions for possible gapless phases for the four-by-four Hamiltonian $H_0 + H_{AFM}$, which is discussed in Sec.III A in the main text to understand the phase diagram of the above Hamiltonian. Without antiferromagnetic ordering, the energy dispersion of the Luttinger Hamiltonian H_0 possesses a quadratic touching at the Γ point. With the AFM term (at least one nonzero ξ_i for $i \neq 0$), the Hamiltonian $H_0 + H_{AFM}$ can be analytically solved (Eq.8). The requirement for a gapless point is that $h_i(\mathbf{k}) + \xi_i = 0$ for all $i = 1, 2, \ldots, 5$ for a certain momentum $\mathbf{k}$. Below we will list all the possible cases for a gapless point to exist in the momentum space. Here $\beta_c, \gamma_2, \gamma_3 \neq 0$ are always assumed.

Case I: $\xi_3 = \xi_4 = \xi_5 = 0$.

In this case, we require $h_3 = h_4 = h_5 = 0$. According to the form of $h_{3,4,5}$, we immediately see that two of three components of the momentum (k_x, k_y, k_z) should be zero. Let us assume $k_x = k_y = 0$ and for the remaining nonzero k_z, we still need to solve two equations $h_1 = -\xi_1$ and $h_2 = -\xi_2$. This suggests that ξ_1 and ξ_2 cannot be independent of each other in order to achieve a gapless phase. According to the form of $h_{1,2}$, we find gapless points at

$$\mathbf{k}a = (0, 0, \pm\sqrt{-\frac{\xi_1}{2\beta_c\gamma_2}})$$

for $\xi_3 = \xi_4 = \xi_5 = 0, \xi_2 = 0, \xi_1\beta_c\gamma_2 < 0$.

Similarly, if $k_y = k_z = 0$, we have gapless points at

$$\mathbf{k}a = \pm(\sqrt{-\frac{\xi_2}{\sqrt{3}\beta_c\gamma_2}}, 0, 0)$$

for $\xi_3 = \xi_4 = \xi_5 = 0, \xi_2\beta_c\gamma_2 < 0, \xi_2 = -\sqrt{3}\xi_1$.

And if $k_x = k_z = 0$, we have gapless points at

$$\mathbf{k}a = \pm(0, \sqrt{\frac{\xi_2}{\sqrt{3}\beta_c\gamma_2}}, 0)$$

for $\xi_3 = \xi_4 = \xi_5 = 0, \xi_2\beta_c\gamma_2 > 0, \xi_2 = \sqrt{3}\xi_1$.

Case II: For ξ_3, ξ_4 and ξ_5, two of them are zero and one is non-zero.

For this case, let's take the example of $\xi_3 = \xi_4 = 0$ and $\xi_5 \neq 0$ and the analysis for other cases are similar. Since $\xi_5 \neq 0$, $k_{y,z}$ cannot be zero from $h_5 = -\xi_5$. Therefore, $\xi_3 = \xi_4 = 0$ gives rise to $k_x = 0$. For the remaining three equations $h_{1,2,5} = -\xi_{1,2,5}$, we find only two variables k_y and k_z. Thus, one of $\xi_{1,2,5}$ should depend on the other two. By solving the equations $h_{1,2,5} = -\xi_{1,2,5}$, we find gapless points at

$$\mathbf{k}a = \pm(0, \frac{1}{\sqrt[4]{3}}\sqrt{\frac{\xi_2}{\beta_c\gamma_2}}, -\frac{1}{\sqrt[4]{3}}\sqrt{\frac{\gamma_2\beta_c}{\xi_2}}\frac{\xi_5}{2\gamma_3\beta_c})$$

for $\xi_3 = \xi_4 = 0, \xi_5 \neq 0, \xi_2\gamma_2\beta_c > 0, \xi_1 = \frac{1}{\sqrt{3}}(\xi_2 - \frac{\gamma_2^2\xi_5^2}{2\gamma_3^2\xi_2})$.

Similarly, if $\xi_3 = \xi_5 = 0, \xi_4 \neq 0$, the gapless points are at

$$\mathbf{k}a = \pm(\frac{1}{\sqrt[4]{3}}\sqrt{-\frac{\xi_2}{\beta_c\gamma_2}}, 0, -\frac{1}{\sqrt[4]{3}}\sqrt{-\frac{\beta_c\gamma_2}{\xi_2}}\frac{\xi_4}{2\gamma_3\beta_c})$$

for $\xi_2\gamma_2\beta_c < 0, \xi_1 = -\frac{1}{\sqrt{3}}(\xi_2 - \frac{\gamma_2^2\xi_4^2}{2\gamma_3^2\xi_2})$.

And if $\xi_4 = \xi_5 = 0, \xi_3 \neq 0$, the gapless points are at

$$\mathbf{k}a = \pm(-\frac{\xi_3}{2\sqrt{3}\beta_c\gamma_3}\sqrt{\frac{2\sqrt{3}\beta_c\gamma_2}{\sqrt{3}\xi_1 + \xi_2}}, \sqrt{\frac{\sqrt{3}\xi_1 + \xi_2}{2\sqrt{3}\beta_c\gamma_2}}, 0)$$

for $(\sqrt{3}\xi_1 - \xi_2)\beta_c\gamma_2 > 0, (\sqrt{3}\xi_1 + \xi_2)\beta_c\gamma_2 > 0, \gamma_2^2\xi_3^2 + \gamma_3^2(\xi_2^2 - 3\xi_1^2) = 0$.

Case III: For ξ_3, ξ_4 and ξ_5, one of them is zero and the other two are non-zero.

Gapless points cannot exist for this case. This is because once two of $\xi_{3,4,5}$ are nonzero, none of three components $k_{x,y,z}$ of a gapless point can be zero. Thus, the other ξ should also be non-zero for gapless points to exist.

Case IV: All three $\xi_{3,4,5}$ are non-zero.

For this case, we need to solve five equations $h_i = -\xi_i$ $(i = 1, \ldots, 5)$ with three variables $k_{x,y,z}$. Therefore, only three of the five ξ's are independent. Let's assume $\xi_{3,4,5}$ are independent variables and one can first solve three equations $h_{3,4,5} = -\xi_{3,4,5}$ for the momentum (k_x, k_y, k_z) to get possible positions of gapless points , and then plug them in $\xi_{1,2} = -h_{1,2}$ to get the relation between ξ_1 and ξ_2 and the exact possible positions. Results are listed below.

If $\xi_3 \neq 0, \xi_4 \neq 0, \xi_5 \neq 0, \xi_3\xi_4\xi_5\beta_c\gamma_3 < 0, \xi_3\beta_c\gamma_3 < 0, \xi_4\beta_c\gamma_3 < 0, \xi_5\beta_c\gamma_3 < 0, \xi_2 = \frac{\gamma_2\xi_3(\xi_4-\xi_5)(\xi_4+\xi_5)}{2\gamma_3\xi_4\xi_5}, \xi_1 = -\frac{\gamma_2(\xi_3^2\xi_4^2+\xi_3^2\xi_5^2-2\xi_4^2\xi_5^2)}{2\sqrt{3}\gamma_3\xi_3\xi_4\xi_5}$, the gapless points are located at

$$\mathbf{k}a = \pm\frac{1}{\sqrt{2}\sqrt[4]{3}}(\sqrt{-\frac{\xi_3\xi_4}{\beta_c\gamma_3\xi_5}}, \sqrt{-\frac{\xi_3\xi_5}{\beta_c\gamma_3\xi_4}}, \sqrt{-\frac{\xi_4\xi_5}{\beta_c\gamma_3\xi_3}})$$

.

If $\xi_3 \neq 0, \xi_4 \neq 0, \xi_5 \neq 0, \xi_3\xi_4\xi_5\beta_c\gamma_3 < 0, \xi_3\beta_c\gamma_3 < 0, \xi_4\beta_c\gamma_3 > 0, \xi_5\beta_c\gamma_3 > 0, \xi_2 = \frac{\gamma_2\xi_3(\xi_4-\xi_5)(\xi_4+\xi_5)}{2\gamma_3\xi_4\xi_5}, \xi_1 = -\frac{\gamma_2(\xi_3^2\xi_4^2+\xi_3^2\xi_5^2-2\xi_4^2\xi_5^2)}{2\sqrt{3}\gamma_3\xi_3\xi_4\xi_5}$, the gapless points are

$$\mathbf{k}a = \pm\frac{1}{\sqrt{2}\sqrt[4]{3}}(\sqrt{-\frac{\xi_3\xi_4}{\beta_c\gamma_3\xi_5}}, \sqrt{-\frac{\xi_3\xi_5}{\beta_c\gamma_3\xi_4}}, -\sqrt{-\frac{\xi_4\xi_5}{\beta_c\gamma_3\xi_3}})$$

.

If $\xi_3 \neq 0, \xi_4 \neq 0, \xi_5 \neq 0, \xi_3\xi_4\xi_5\beta_c\gamma_3 < 0, \xi_3\beta_c\gamma_3 > 0, \xi_4\beta_c\gamma_3 < 0, \xi_5\beta_c\gamma_3 > 0, \xi_2 = \frac{\gamma_2\xi_3(\xi_4-\xi_5)(\xi_4+\xi_5)}{2\gamma_3\xi_4\xi_5}, \xi_1 = -\frac{\gamma_2(\xi_3^2\xi_4^2+\xi_3^2\xi_5^2-2\xi_4^2\xi_5^2)}{2\sqrt{3}\gamma_3\xi_3\xi_4\xi_5}$, the gapless points are

$$\mathbf{k}a = \pm\frac{1}{\sqrt{2}\sqrt[4]{3}}(\sqrt{-\frac{\xi_3\xi_4}{\beta_c\gamma_3\xi_5}}, -\sqrt{-\frac{\xi_3\xi_5}{\beta_c\gamma_3\xi_4}}, \sqrt{-\frac{\xi_4\xi_5}{\beta_c\gamma_3\xi_3}})$$

.

If $\xi_3 \neq 0, \xi_4 \neq 0, \xi_5 \neq 0, \xi_3\xi_4\xi_5\beta_c\gamma_3 < 0, \xi_3\beta_c\gamma_3 > 0, \xi_4\beta_c\gamma_3 > 0, \xi_5\beta_c\gamma_3 < 0, \xi_2 = \frac{\gamma_2\xi_3(\xi_4-\xi_5)(\xi_4+\xi_5)}{2\gamma_3\xi_4\xi_5}, \xi_1 = -\frac{\gamma_2(\xi_3^2\xi_4^2+\xi_3^2\xi_5^2-2\xi_4^2\xi_5^2)}{2\sqrt{3}\gamma_3\xi_3\xi_4\xi_5}$, the gapless points are

$$\mathbf{k}a = \pm\frac{1}{\sqrt{2}\sqrt[4]{3}}(-\sqrt{-\frac{\xi_3\xi_4}{\beta_c\gamma_3\xi_5}}, \sqrt{-\frac{\xi_3\xi_5}{\beta_c\gamma_3\xi_4}}, \sqrt{-\frac{\xi_4\xi_5}{\beta_c\gamma_3\xi_3}})$$

.

D. Dirac Point With Mirror Symmetry

In this section, we will consider the low energy effective theory around the gapless points of the Hamiltonian $H_0 + H_{AFM}$ and show it can be described by a Dirac Hamiltonian for the parameter choices discussed in the Sec.III A in the main text. Here we consider a generic gapless point (K_p, K_p, K_z) in the momentum space, which exist on a mirror or glide plane. We expand the momentum around these gapless points with $(k_x, k_y, k_z) \equiv (K_p + q_x, K_p + q_y, K_z + q_z)$ where $q_{x,y,z}$ are assumed to take small numbers for perturbation. By expanding $H_D \equiv H_0 + H_{AFM}$ around the gapless points (K_p, K_p, K_z) to the first order of q_i's, we obtain

$$H_D(K_p+q_x, K_p+q_y, K_z+q_z) \approx \Gamma_0 + q_x\Gamma_x + q_y\Gamma_y + q_z\Gamma_z,$$

where $\Gamma_0 = \frac{4}{15}[E_v + \xi_0 - 2\beta_c\gamma_1K_p^2 - \beta_c\gamma_1K_z^2](J_x^2 + J_y^2 + J_z^2)$,

$\Gamma_x \equiv -\frac{2}{3}\beta_c\gamma_2 K_p(2J_z^2 - J_x^2 - J_y^2) + 2\beta_c\gamma_2 K_p(J_x^2 - J_y^2) + 4\beta_c\gamma_3 K_p J_{xy} + 4\beta_c\gamma_3 K_z J_{zx}$,
$\Gamma_y \equiv -\frac{2}{3}\beta_c\gamma_2 K_p(2J_z^2 - J_x^2 - J_y^2) - 2\beta_c\gamma_2 K_p(J_x^2 - J_y^2) + 4\beta_c\gamma_3 K_p J_{xy} + 4\beta_c\gamma_3 K_z J_{yz}$, and
$\Gamma_z \equiv +\frac{4}{3}\beta_c\gamma_2 K_z(2J_z^2 - J_x^2 - J_y^2) + 4\beta_c\gamma_3 K_p J_{zx} + 4\beta_c\gamma_3 K_p J_{yz}$.

Since $\beta_c, \gamma_2, \gamma_3 \neq 0$ and K_p, K_z cannot be zero at the same time, none of Γ_x, Γ_y and Γ_z are vanishing. Let us define $q_1 \equiv q_x + a_1 q_y + a_2 q_z$, $q_2 \equiv q_y + a_3 q_z$, $q_3 \equiv q_z$, $\Gamma_1 \equiv \Gamma_x$, $\Gamma_2 \equiv -a_1\Gamma_x + \Gamma_y$, $\Gamma_3 \equiv -a_3\Gamma_x - a_3\Gamma_y + \Gamma_z$ with $a_1 \equiv \frac{K_p^2(3\gamma_3^2 - 2\gamma_2^2)}{4\gamma_2^2 K_p^2 + 3\gamma_3^2(K_p^2 + K_z^2)}$, $a_3 \equiv \frac{K_p K_z(-2\gamma_2^2 + 3\gamma_3^2)}{2K_p^2(\gamma_2^2 + 3\gamma_3^2) + 3\gamma_3^2 K_z^2}$ and $a_2 \equiv a_3(1 + a_1)$. We find that the Hamiltonian H_D can be re-written as

$$H_D(K_p + q_x, K_p + q_y, K_z + q_z) \approx \Gamma_0 + q_1\Gamma_1 + q_2\Gamma_2 + q_3\Gamma_3,$$

where $\{\Gamma_i, \Gamma_j\} = 0, i \neq j$ and $\{\Gamma_i, \Gamma_i\} \neq 0$ for $i, j = 1, 2, 3$. Thus, we conclude that all gapless points, if exist, are Dirac points with the low energy effective theory described by Dirac fermions, for the parameter choices discussed in the Sec.III A in the main text.

E. C_{3v}^* spin double group

C_{3v}^*	E	R	C_3,C_3^2R	C_3^2, C_3R	$3\sigma_v$	$3\sigma_v$R
Λ_1	1	1	1	1	1	1
Λ_2	1	1	1	1	-1	-1
Λ_3	2	2	-1	-1	0	0
Λ_4	1	-1	-1	1	i	-i
Λ_5	1	-1	-1	1	-i	i
Λ_6	2	-2	1	-1	0	0

TABLE V. Character Table of Spin Double Group C_{3v}^* [69]

This section shows how four bases of Γ_8 bands can be constructed into $\Lambda_{4,5,6}$ irreducible representations of C_{3v}^* spin double group, as discussed in Sec.III D. The character table of C_{3v}^* spin double group is shown in Tab.V. Wave functions for each irreducible representations in bases $|\Gamma_8, 3/2\rangle$, $|\Gamma_8, 1/2\rangle$, $|\Gamma_8, -1/2\rangle$ and $|\Gamma_8, -3/2\rangle$ are shown below:

Λ_4:

$$N_4\left(\frac{1-i}{\sqrt{2}}, \frac{\sqrt{2}-i}{\sqrt{3}}, i\left(\frac{1}{\sqrt{6}} + \frac{1}{\sqrt{3}}\right) - \sqrt{\frac{1}{6}\left(3 - 2\sqrt{2}\right)}, 1\right)$$

Λ_5:

$$N_5\left(\frac{-1+i}{\sqrt{2}}, -\frac{\sqrt{2}+i}{\sqrt{3}}, i\sqrt{\frac{1}{6}\left(3 - 2\sqrt{2}\right)} - \frac{1}{\sqrt{3}} - \frac{1}{\sqrt{6}}, 1\right)$$

Λ_6:

$$\frac{1}{\sqrt{6}}\left(-1 - i, i\sqrt{3}, 0, 1\right), \frac{1}{\sqrt{6}}\left(i\sqrt{3}, 1 - i, 1, 0\right)$$

,where N_4 and N_5 are normalization factors.

F. Tables for Parameters

This section is devoted to a summary of all the parameters for the four-band model and the extended Kane model used throughout the main text of the manuscript.

$\frac{E_v+\xi_0}{\varepsilon_0}$	γ_1	γ_2	γ_3	$\frac{C}{\beta_c/a}$	$\frac{\xi_2}{\varepsilon_0}$	$\frac{\xi_1}{\varepsilon_0}$
0	0	0.5	0.1	0	0	−0.16

TABLE VI. Choices of parameters for Fig.2a. $\xi_4 = \xi_5$, $\xi_3/\varepsilon_0 \in [-0.3, 0.3]$ and $\xi_4/\varepsilon_0 \in [-0.3, 0.3]$, where a is a real parameter with the unit of length.

$\frac{E_v+\xi_0}{\varepsilon_0}$	γ_1	γ_2	γ_3	$\frac{C}{\beta_c/a}$	$\frac{\xi_2}{\varepsilon_0}$	$\frac{\xi_1}{\varepsilon_0}$
0	0	0.5	0.1	0.2	0	−0.16

TABLE VII. Choices of parameters for Fig.3a. $\xi_4 = \xi_5$, $\xi_3/\varepsilon_0 \in [-0.3, 0.3]$ and $\xi_4/\varepsilon_0 \in [-0.3, 0.3]$.

$\frac{E_v+\xi_0}{\varepsilon_0}$	γ_1	γ_2	γ_3	$\frac{C}{\beta_c/a}$	$\frac{\xi_2}{\varepsilon_0}$	$\frac{\xi_3}{\varepsilon_0}$	$\frac{\xi_4}{\varepsilon_0}$	$\frac{\xi_1}{\varepsilon_0}$
0	0	1	0.5	0.2	0	0	0.1	0.7

TABLE VIII. Choices of parameters for Fig.5. $\xi_4 = \xi_5$.

$\frac{E_v+\xi_0}{\varepsilon_0}$	γ_1	γ_2	γ_3	$\frac{C}{\beta_c/a}$	$\frac{\xi_2}{\varepsilon_0}$	$\frac{\xi_1}{\varepsilon_0}$	$\frac{\xi}{\varepsilon_0}$
0	0	0.5	0.1	0.2	0	0	−0.025

TABLE IX. Choices of parameters for Fig.6. $\xi_3 = \xi_4 = \xi_5 \equiv \xi$.

$\frac{E_c}{\varepsilon_0}$	$\frac{E_v+\xi_0}{\varepsilon_0}$	γ_1	γ_2	γ_3	$\frac{C}{\beta_c/a}$	$\frac{P}{\beta_c/a}$
−2	0	$2+\delta$	$0.5+\frac{\delta}{2}$	$0.1+\frac{\delta}{2}$	0.2	1
$\frac{\xi_3}{\varepsilon_0}$	$\frac{\xi_4}{\varepsilon_0}$	$\frac{\xi_3}{\varepsilon_0}$	B_{8v}^+/β_c	B_{8v}^-/β_c		
0	0	0	0	0		

TABLE X. Choices of parameters for Fig.7a. Here $\delta \equiv \frac{P^2}{3(E_v+\xi_0-E_c)\beta_c}$, $\xi_1/\varepsilon_0 \in (-0.9, 0.9)$, $\xi_2/\varepsilon_0 \in (-0.9, 0.9)$.

$\frac{E_c}{\varepsilon_0}$	$\frac{E_v+\xi_0}{\varepsilon_0}$	γ_1	γ_2	γ_3	$\frac{C}{\beta_c/a}$	$\frac{P}{\beta_c/a}$
−2	0	$2+\delta$	$0.5+\frac{\delta}{2}$	$0.1+\frac{\delta}{2}$	0.2	1
$\frac{\xi_2}{\varepsilon_0}$	$\frac{\xi_4}{\varepsilon_0}$	$\frac{\xi_3}{\varepsilon_0}$	B_{8v}^+/β_c	B_{8v}^-/β_c		
0	0	0	0	0		

TABLE XI. Choices of parameters for Fig.7b. Here $\delta \equiv \frac{P^2}{3(E_v+\xi_0-E_c)\beta_c}$, $\xi_1/\varepsilon_0 \in (-0.9, 0.9)$, $\xi_3/\varepsilon_0 \in (-0.9, 0.9)$.

$\frac{E_c}{\varepsilon_0}$	$\frac{E_v+\xi_0}{\varepsilon_0}$	γ_1	γ_2	γ_3	$\frac{C}{\beta_c/a}$	$\frac{P}{\beta_c/a}$
-2	0	$2+\delta$	$0.5+\frac{\delta}{2}$	$0.1+\frac{\delta}{2}$	0.2	1
$\frac{\xi_3}{\varepsilon_0}$	$\frac{\xi_4}{\varepsilon_0}$	$\frac{\xi_3}{\varepsilon_0}$	B_{8v}^+/β_c	B_{8v}^-/β_c		
-0.01	0.023	0.026	0	0		

TABLE XII. Choices of parameters for Fig.8a.Here $\delta \equiv \frac{P^2}{3(E_v+\xi_0-E_c)\beta_c}$, $\xi_1/\varepsilon_0 \in (-0.9, 0.9)$, $\xi_2/\varepsilon_0 \in (-0.9, 0.9)$ and the choice of (ξ_3, ξ_4, ξ_5) breaks the symmetry group C_{3v} and its combination with $T_{\mathbf{a}_3'}$.

G. Determination of Critical Lines in Fig.3a

The section describes how to determine critical lines in Fig.3a in the main text.

First, we hope to demonstrate that the Weyl points are from the Π pairs on the $(1\bar{1}0)$ plane in our case. The creation or annihilation of Weyl points requires two Weyl points with opposite Chern numbers, thus only occuring between a Π pair(like along path γ) or a ΠS pair for the case described in Sec.III(b). If a ΠS pair merges, it can only happen on the $(1, -1, 0)$ axis where the Hamiltonian is invariant under $\pi_{1\bar{1}0}S$ and each band is doubly degenerate. If Hamiltonian is gapless at some point on the $(1, -1, 0)$ axis, say $(k', -k', 0)$, it requires the Hamiltonian to be an identity at that point, and implies that $\xi_4 = 0$, $Ck' = 0$, $\xi_3 = 2\sqrt{3}\beta_c\gamma_3 k'^2$ and $\xi_1 = 2\beta_c\gamma_2 k'^2$. Since $C \neq 0$ and $\sum_{i=1,,5} \xi_i^2 \neq 0$, the Hamiltonian cannot be gapless on the $(1, -1, 0)$ axis, and therefore Weyl points cannot exist on the $(1, -1, 0)$ axis. We conclude Weyl points can only originate from the Π pairs on the $(1\bar{1}0)$ plane for the parameter regions that we are interested in.

When Weyl points are away from the mirror $(1\bar{1}0)$ plane, energy bands are gapped in the $(1\bar{1}0)$ plane, where the mirror Chern number is well-defined and can be computed to be 1. Thus, the mirror Chern number provides additional characterization of topological property in our system. The mirror Chern number always changed by 1 between the transition from the phase I to II or from II to III in Fig. 3(a). This suggests that band gap closing at the transition lines should occur between two bands in one mirror (or glide) subspace. This allows us to determine the phase transition lines (blue lines in Fig. 3(a)) by solving gapless condition of a mirror (or glide) subspace:

$$48\beta_c\gamma_3^2\xi_3^2\xi_1 + \left(\xi_4^2 - \xi_3^2\right)\left(C \pm \sqrt{C^2 - 16\sqrt{3}\beta_c\gamma_c\xi_3}\right)^2 = 0.$$